



NRL/MR/6040--15-9630

Numerical Study of Noise Characteristics in Overexpanded Jet Flows

JUNHUI LIU

ANDREW CORRIGAN

K. KAILASANATH

*Laboratories for Computational Physics and Fluid Dynamics
Materials Science and Component Technology Directorate*

NICHOLAS HEEB

EPHRAIM GUTMARK

*University of Cincinnati
Cincinnati, Ohio*

August 5, 2015

REPORT DOCUMENTATION PAGE				Form Approved OMB No. 0704-0188	
Public reporting burden for this collection of information is estimated to average 1 hour per response, including the time for reviewing instructions, searching existing data sources, gathering and maintaining the data needed, and completing and reviewing this collection of information. Send comments regarding this burden estimate or any other aspect of this collection of information, including suggestions for reducing this burden to Department of Defense, Washington Headquarters Services, Directorate for Information Operations and Reports (0704-0188), 1215 Jefferson Davis Highway, Suite 1204, Arlington, VA 22202-4302. Respondents should be aware that notwithstanding any other provision of law, no person shall be subject to any penalty for failing to comply with a collection of information if it does not display a currently valid OMB control number. PLEASE DO NOT RETURN YOUR FORM TO THE ABOVE ADDRESS.					
1. REPORT DATE (DD-MM-YYYY) 05-08-2015		2. REPORT TYPE Memorandum Report		3. DATES COVERED (From - To) July 2014 – March 2015	
4. TITLE AND SUBTITLE Numerical Study of Noise Characteristics in Overexpanded Jet Flows				5a. CONTRACT NUMBER	
				5b. GRANT NUMBER	
				5c. PROGRAM ELEMENT NUMBER	
6. AUTHOR(S) Junhui Liu, Andrew Corrigan, K. Kailasanath, Nicholas Heeb, ¹ and Ephraim Gutmark ¹				5d. PROJECT NUMBER 64-9290-C5	
				5e. TASK NUMBER	
				5f. WORK UNIT NUMBER	
7. PERFORMING ORGANIZATION NAME(S) AND ADDRESS(ES) Naval Research Laboratory, Code 6041 Laboratory for Propulsion, Energetics, and Dynamic Systems 4555 Overlook Avenue, SW Washington, DC 20375-5320				8. PERFORMING ORGANIZATION REPORT NUMBER NRL/MR/6040--15-9630	
9. SPONSORING / MONITORING AGENCY NAME(S) AND ADDRESS(ES) Office of Naval Research 875 N. Randolph Street, Suite 1425 Arlington, VA 22203-1995				10. SPONSOR / MONITOR'S ACRONYM(S) ONR	
				11. SPONSOR / MONITOR'S REPORT NUMBER(S)	
12. DISTRIBUTION / AVAILABILITY STATEMENT Approved for public release; distribution is unlimited.					
13. SUPPLEMENTARY NOTES ¹ University of Cincinnati, Cincinnati, Ohio 45221-0070					
14. ABSTRACT Noise characteristics in shock-containing jets at an overexpanded jet condition have been investigated. Total temperature ratios of 1.0 (cold), 2.0, and 3.0 are considered. The cold jet is a highly screeching jet. Frequency-wavenumber Fourier analysis is employed to examine the wave characteristics of pressure waves along the lip line and also along a near-field conical surface. It is found that the radiating portion of the pressure wave intensity increases with the jet temperature, but the hydrodynamic portion is much less sensitive to the change of the jet temperature. The near-field noise intensity associated with the Mach wave radiation is observed over a large axial distance, and the Mach wave radiation extends to much higher frequencies in heated jets. The peak radiation direction in the cold jet is dominated by the axisymmetric mode, but the directions around the sideline show a much weaker azimuthal dependence. Furthermore, the axial locations of lip-line pressure peak intensities at the screech frequency are near the axial locations of shock-cell tips. A reinforcing loop between upstream/downstream propagating waves and the induced shock-cell coherent oscillatory motion is observed in the highly screeching jet. The formation of this reinforcing loop requires a match of the peak phase velocities between upstream and downstream propagating waves. This phase velocity match exists in the highly screeching cold jet, but not in the weakly screeching heated jets. It appears that the phase velocity match that sustains the reinforcing loop is important to the screech generation, and the phase velocity mismatch in heated jets is believed to be an important cause of the screech intensity reduction.					
15. SUBJECT TERMS Computational fluid dynamics (CFD) Shock-associated broadband noise Military flight noise Large-eddy simulations Screech tone Supersonic jet flows Jet noise Mixing noise Nozzle flows					
16. SECURITY CLASSIFICATION OF:			17. LIMITATION OF ABSTRACT	18. NUMBER OF PAGES	19a. NAME OF RESPONSIBLE PERSON
a. REPORT Unclassified Unlimited	b. ABSTRACT Unclassified Unlimited	c. THIS PAGE Unclassified Unlimited			Junhui Liu
			Unclassified Unlimited	46	19b. TELEPHONE NUMBER (include area code) (202) 767-6590

CONTENTS

I. INTRODUCTION	1
II. NOZZLE GEOMETRY AND COMPUTATIONAL DOMAIN	2
III. RESULTS AND DISCUSSIONS	2
A. Noise Distributions in Near Field and Far Field	3
B. Frequency and Wavenumber Analysis	5
C. Noise Characteristics in Azimuthal and Axial Space	9
D. Noise Source of Screech Tones	10
IV. CONCLUSIONS	14
ACKNOWLEDGEMENTS	15
REFERENCES	15
FIGURES	19

EXECUTIVE SUMMARY

Noise characteristics in shock-containing jets at an overexpanded jet condition have been investigated. Total temperature ratios of 1.0 (cold), 2.0, and 3.0 are considered. The cold jet is a highly screeching jet. Frequency-wavenumber Fourier analysis is employed to examine the wave characteristics of pressure waves along the lip line and also along a near-field conical surface. It is found that the radiating portion of the pressure wave intensity increases with the jet temperature, but the hydrodynamic portion is much less sensitive to the change of the jet temperature. The near-field noise intensity associated with the Mach wave radiation is observed over a large axial distance, and the Mach wave radiation extends to much higher frequencies in heated jets. The peak radiation direction in the cold jet is dominated by the axisymmetric mode, but the directions around the sideline show a much weaker azimuthal dependence. Furthermore, the axial locations of lip-line pressure peak intensities at the screech frequency are near the axial locations of shock-cell tips. A reinforcing loop between upstream/downstream propagating waves and the induced shock-cell coherent oscillatory motion is observed in the highly screeching jet. The formation of this reinforcing loop requires a match of the peak phase velocities between upstream and downstream propagating waves. This phase velocity match exists in the highly screeching cold jet, but not in the weakly screeching heated jets. It appears that the phase velocity match that sustains the reinforcing loop is important to the screech generation, and the phase velocity mismatch in heated jets is believed to be an important cause of the screech intensity reduction.

NUMERICAL STUDY OF NOISE CHARACTERISTICS IN OVEREXPANDED JET FLOWS

I. INTRODUCTION

Engine exhausts of high performance supersonic military aircraft during takeoff or landing are shock-containing hot jets, which produce high-intensity jet noise that can have a direct impact on shipboard health and safety issues. Therefore, understanding the noise generation mechanism of shock-containing jets at various jet temperatures is important to the development and optimization of effective noise reduction techniques for military aircraft. The jet noise generated in shock-containing jet flows includes shock-associated noise and mixing noise. The shock-associated noise has discrete tones (screech) and a broadband noise component. The noise generation mechanism in shock-containing jet flows have been experimentally and theoretically investigated by a number of authors in the past [1]-[17]. The early investigations have laid a solid foundation for improving the understanding of the noise characteristics in shock-containing supersonic jet flows. We have examined the noise characteristics of jet flows at an underexpanded jet condition previously in Ref. [18], and have studied the correlation between the near-field acoustic pressure waves and the turbulence fluctuations in the jet plume in Refs [19]. In this paper, we investigate the noise characteristics in jet flows at an overexpanded condition. The cold jet and two heated jets are considered. The cold overexpanded jet is highly screeching, and the two heated jets are used to investigate the heating impact on the screech intensity and also on the Mach wave radiation.

High-intensity screech tones have a large impact on the jet flow and jet turbulence. They disrupt the jet core and increase both the jet turbulence level and the far-field noise level. The noise generation mechanism of screech tones has been the subject of many experimental, theoretical and numerical studies more than half a century. Some examples can be found in Refs [20]-[38]. It was suggested that screech tones were generated and driven by a feedback loop between the flow disturbances inside the jet and the feedback sound waves outside the jet [20]. The screech frequency has been well predicted [21], but the prediction of the screech intensity is elusive. It is found that screech tones present modal behavior, which varies with the jet Mach number. This modal behavior is found to correlate with the modes of the highly amplified instability waves [21]. Large coherent shock-cell oscillatory motion has also been observed in highly screeching jets as reported in Refs [22]-[25]. It was suggested that the coherent shock-cell oscillatory motion could be important to the screech tone generation [23]. It is also found that the screech intensity decreases in hot jets. The frequency mismatch between screech tones and the most amplified instability waves was speculated as the cause of the screech tone reduction in hot jets [21]. On the other hand, Mach wave radiation is generated by instability waves that travel supersonically relative to the ambient sound. It is a dominant noise generation mechanism in high-speed jets. This noise generation mechanism has also been investigated extensively in the past, for example in Refs [39]-[43]. The growth, decay and propagation of the most amplified instability frequencies were examined and modeled. Mach wave radiation suppression techniques were also explored [40].

The total temperature ratios studied in this paper are $TTR = 1.0, 2.0$, and 3.0 . TTR stands for the ratio between the total temperature at the nozzle inlet and the ambient temperature. The Oertel Mach number [44] of these three jets ranges from 1.12, 1.34 and 1.46. It was suggested in Ref. [41] that Mach wave radiation should be a significant component of radiation noise if Oertel Mach number is above 1.25. Thus, we would expect significant Mach wave radiation in the two heated jets. Large-eddy simulations (LES) are used to generate the near-field data. The LES methodology is similar to those reported in our previous work in Refs [18][19], where an unsteady compressible flow solver embedded in the Jet Engine Noise Reduction (JENRE) code was used. This flow solver employs the Finite Element Flux Corrected Transport method [45]-[48], which combines the Taylor-Galerkin finite element method together with the Flux-Corrected Transport convection scheme [45][46] and the Zalesak multi-dimensional flux limiter

[48]. These simulations are in the category of Monotonically Integrated Large-Eddy Simulation approach, which is often addressed as MILES approach. In addition, the far-field noise intensities are predicted by using the Ffowcs Williams & Hawkings (FW-H) integration equation [49] based on the near-field LES results. The flow field and the noise characteristics in both the near and far field are examined. Wave characteristics associated with near-field pressure waves are examined by using the frequency-wavenumber Fourier analysis. This approach has been used by a number of authors to separate the radiating pressure waves from the hydrodynamic non-radiation pressure fluctuations in the jet plume, for example in Refs [50]-[53]. Difficulties associated with this approach were also presented in Ref. [53]. In addition, azimuthal dependence of both screech tones and Mach wave radiation are examined. The noise source associated with screech tones are investigated.

II. NOZZLE GEOMETRY AND COMPUTATIONAL DOMAIN

The nozzle geometry for the shock-containing jet flows is shown in Figure 1. It is a representative of practical military engine nozzles, similar to that used in Refs [18][19]. The design Mach number M_d of this C-D nozzle is 1.5, and the fully expanded pressure ratio is 3.7. Figure 2(a) shows the computational domain, where the near-field useful region is enclosed by the nozzle surfaces and the funnel-shaped surface colored in grey. Again, the grid resolution and the computational domain is the same as those reported in Refs [18][19]. The axial range of the funnel-shaped surface extends from 2.0D (D is the nozzle exit diameter) upstream of the nozzle exit to 27.0D downstream. The upstream portion has a radius of 1.5D, but the downstream portion is 9.5° to the jet axis. The cell size is around $D/286.0$ in the shear layer, and gradually increases to a size around $D/30.0$ in the axial direction as shown in Fig. 2(b). In addition, the cell size of $D/30.0$ extends to the remaining portion of the region enclosed by the black lines shown in Figure 2(a). The radius of this region is 1.1D above the nozzle exit and 1.8D from $x = 10.0D$ to 25.0D. Furthermore, the cell size gradually increases to a size around $D/20.0$ in the region near the conical surface, beyond which the cell size increases rapidly to a very large size in the far field. Overall the simulation domain extends to 30.0D in the radial direction, 17.0D upstream of the nozzle exit and 70.0D downstream in the axial direction. A buffer zone is implemented near the far-field boundaries to remove the wave reflection, and the number of grid points is 59 millions.

III. RESULTS AND DISCUSSIONS

The jet flows in this paper are overexpanded with a nozzle pressure ratio of 3.5 and jet Mach number (M_j) of 1.47. The off-design intensity $\beta = \sqrt{|M_j^2 - M_D^2|}$ is 0.23, which is somewhat lower than the off-design intensity ($\beta = 0.42$) of underexpanded jet flows reported in our previous study [18][19]. Thus the contribution of the shock-associated broadband noise would be expected to be smaller than that in the underexpanded jets in our previous study. However, the cold overexpanded jet is highly screeching, whereas the underexpanded jets only have a weak screech tone. Similar to the practice used in Refs [18][19], shock-free jets that have similar jet velocities are also simulated to distinguish the contribution of the shock-associated noise component.

Figure 3 shows the time-averaged streamwise velocity distributions for these three overexpanded jets, and Figure 4 shows the centerline axial velocity distributions of both shock-containing and shock-free jets. It can be seen that the jet core length in the overexpanded cold jet is shorter than that in the shock-free cold jet, but this difference is substantially reduced as the jet temperature increases. The jet core lengths in shock-free jets are 9.3D, 8.1D, and 7.7D at TTR of 1.0, 2.0, and 3.0, respectively. The jet core length of the overexpanded cold jet is roughly 8.1D, so it is more than one jet diameter shorter than that of the shock-free jet. In addition, the change of the jet temperature has no impact on the shock-cell structure upstream of the shock-cell decay region. This is also true in the underexpanded jet flows reported in Ref.

[18]. Furthermore, Figure 5 shows the time-averaged turbulence kinetic energy distributions along both the centerline and the lip line. It can be seen that the turbulence kinetic energy along the centerline in the cold overexpanded jet is much higher than that in the shock-free jet, but this centerline difference is also getting smaller as the jet temperature increases. The shock-cell impact on the centerline distributions in the two heated jets is similar to that in the mildly screeching underexpanded jets [18]. On the other hand, the impact on the lip line is much smaller, except that the shock-cell impact in the cold jet is slightly larger than that in the two heated jets. The highly screeching underexpanded jets reported in Ref. [12] also show a large increase of the lip-line turbulence besides the large increase in the centerline. This different impact of the screech tone on the lip-line turbulence probably is related to the difference between the overexpanded and underexpanded jet conditions. An overexpanded jet core would have a smaller jet core width and the high-speed portion of the shear layer would fall off the lip line faster. This makes the velocity and velocity gradient along the lip line smaller than those that would be observed in underexpanded jets.

A. Noise Distributions in both Near Field and Far Field

The funnel-shaped surface shown in Figure 2(a) is used as FW-H surface for the far-field prediction. The quality of FW-H surface has been carefully assessed in Ref. [19], and it was shown that both the radial and axial locations of the current FW-H surface are appropriate for the far-field prediction. In addition, the total temporal sample length of LES data used for the spectral analysis is around $900 D/U_j$, which is divided into six windows with a 50% overlap between windows. This results in 11 windows and each window has 4096 bins. Figure 6 shows the sound pressure level (SPL) distributions on the FW-H surface in the overexpanded cold jet and the overall sound pressure levels (OASPL) in both the shock-containing and shock-free cold jets. It can be seen that a strong fundamental screech tone (the first screech harmonic) and the second screech harmonic tone are observed in this overexpanded jet. It appears that there is also a higher screech harmonic tone, but its intensity is much weaker. The screech frequencies agree very well with the measurement data, and the screech intensities are also comparable to those observed in measurements. The strong screech tone causes a large modulation on the OASPL distribution upstream of $x = 6D$ and greatly increase the sound pressure level near the nozzle exit. The small peak level around $x = 7D$ is contributed by the second screech harmonic. In addition, shock cells elevate the pressure fluctuation level in the region up to $x = 15D$ on the FW-H surface, but very little difference is observed further downstream. This is similar to that observed in the mildly screeching underexpanded cold jet reported in Ref. [18].

Figure 7 shows SPL contour distributions along the conical surface shown in Figure 2(a). Both the overexpanded and shock-free cold jets and the heated overexpanded jet at $TTR = 2.0$ are shown. It can be seen that the shock-free distribution is dominated by the large-scale contribution, and the dominant noise source starts from around $x = 5D \sim 6D$. When shock cells are present, the shock-associated broadband component is clearly observed in the middle frequency range. The shock-associated broadband peak frequency increases in the downstream direction, similar to that reported in the underexpanded jets in Ref. [18], and it has been also observed in several measurements as shown in Refs. [8][15][16]. The fundamental screech tone can be seen over a large axial distance, but the largest magnitude is found upstream of $x = 5D$. In addition, there are also two higher screech harmonics shown in Figure 7(b), where the second harmonic is roughly between $x = 5D \sim 10D$ and centered around $x = 7D$. The third harmonic is found between $x = 6D \sim 9D$, but is much weaker and barely visible in this figure. In addition, the low-frequency intensity is higher in the overexpanded cold jet than that in the shock-free jet. Increasing the jet temperature increases the overall noise level, but the screech intensity is reduced, so is the low-frequency component. In addition, the screech higher harmonics disappear in the heated jet. Furthermore, the heating impact on the screech intensity is examined in Figure 8, where SPL distributions at the location of $1.5D$ above the nozzle exit are shown. Distributions from the mildly screeching underexpanded cold jet taken from Ref. [18] are also presented in this figure. It can be seen that in both the overexpanded and the underexpanded jets, increasing the jet temperature increases the screech frequency, but decreases the

screech Strouhal number. The overexpanded jets show a reduction of the screech intensity with the jet temperature, but the screech intensity in the underexpanded jets is not sensitive to the change of the jet temperature. Thus, the heating effect on the screech intensity in the strong screeching overexpanded jet is different from that in the mildly screeching underexpanded jet. In addition, there is a low-frequency peak in the range between $St = 0.1$ and 0.2 shown in all overexpanded and underexpanded jets. The frequency and Strouhal number of this low-frequency peak respond to the change of the jet temperature in a similar way to those of screech tones, except that the frequency decreases faster than the screech frequency. The intensity of the low-frequency peak in the overexpanded jets decreases with the jet temperature, but the trend is opposite in the underexpanded jets. The two heated overexpanded jets do not show screech harmonics, but they present a small shock-associated broadband noise region at frequencies higher than the screech frequency, whereas the shock-associated broadband noise region in the highly screeching cold jet is barely visible at this location. This is consistent with the observation that screech tones suppress the broadband shock-associated noise component [10]. On the other hand, the underexpanded profiles show a more consistent profile around the screech frequency.

Figure 9 shows the far-field SPL and OASPL distributions at a far-field radius of $47D$. The shock-containing results are compared with both the measurement data and also the shock-free results. The frequencies of the fundamental screech tone and its harmonics compare well with measurement data, and the shift of the broadband peak of the shock-associated noise to higher frequencies in the downstream direction is accurately captured. The peak intensity of the fundamental screech tone is in the upstream direction, but the first harmonic tone has the peak intensity near the sideline direction. In addition, the second harmonic tone, which is less visible, can be seen between $60^\circ \sim 70^\circ$ and between $110^\circ \sim 120^\circ$. The radiation directions of these screech harmonics are similar to those shown in the jet flow of $M_j = 1.49$ in Ref. [31]. The far-field OASPL also agrees well with measurement data, and the impact of the screech tone and the second harmonic tone is clearly shown in these distributions. On the other hand, the shock-free jet shows a continuous increase from upstream to downstream. There is almost 13dB difference between the overexpanded and the shock-free jet at the upstream angle of 35° .

Figure 10 shows the OASPL contours from the jet plume to a far-field distance of $r = 100D$ in these three overexpanded jets. The FW-H surface integral method [49] is used to generate the OASPL contours outside the jet plume. In addition, Figure 11 shows the far-field OASPL distributions at the far-field distance $r = 100D$. There are four distinctive peak radiation directions in the pressure wave propagation in the cold jet, and three of them are shock-associated. The one at the angle of 22° in the upstream direction is the fundamental screech tone. The one at the sideline is the second screech harmonic, as we have observed in Figure 9. The small peak between 120° and 130° , however, is contributed by the shock-associated broadband noise, which will be discussed more in the next subsection. The peak at 152.8° , on the other hand, is contributed by the Mach wave radiation. As the jet temperature increases, the screech intensity is largely reduced and the Mach wave radiation becomes much more prominent and its peak radiation direction moves upstream. In addition, the variation of the noise intensity on the upstream side of the peak radiation angle becomes steeper as the jet temperature increases. On the other hand, the variation on the downstream side changes less with the jet temperature. The peak angles at $r = 100D$ are 152.8° , 138.9° , and 129.6° at the jet temperature ratio $TTR = 1.0$, 2.0 and 3.0 , respectively. The peak angles computed from Oertel Mach wave number M'_c (Refs [41][44]) at these jet temperatures are 152.9° , 138.4° , and 133.3° , and Tam's vortex sheet model [31] predicts 140.7° , 132.5° and 129.7° . It can be seen that the peak angles of the first two jet temperatures agree very well with predictions computed from Oertel Mach wave number M'_c , but the peak angle of the heated jet at $TTR = 3.0$ has a better agreement with Tam's vortex sheet model. Furthermore, it is worth noting that the peak radiation angle changes with the far-field distance if the observation point is not sufficiently far from the jet plume, as can be seen in Figure 12. Since the far-field angle is defined as the angle of the line connected the nozzle exit center and the observation point, the radiation angle will vary with the observer's distance if the distance between

the noise source and the nozzle exit center is comparable to the observer's distance. It can be seen that peak radiation angles initially decrease with the radius and then reach saturated values when the distance is sufficiently large. For example, the peak radiation angle associated with Mach wave radiation is roughly 160° at $r = 30D$, 154° at $r = 50D$ and 152.8° at $r = 100D$. The peak radiation angle at $r = 100D$ appears to be very close to the saturated value based on this figure.

Figure 13 shows far-field SPL distributions of both shock-containing and shock-free jets at the cold and a heated jet conditions. It can be seen that increasing the jet temperature reduces the overall impact of shock cells on the total noise, which is similar to the trend we have observed in underexpanded cases in Ref. [18]. In addition, as the jet temperature increases from $TTR = 1.0$ to $TTR = 2.0$, the intensity of the fundamental screech tone is greatly reduced and all screech higher harmonics disappear. In addition, the screech intensity in the cold jet decreases from upstream to downstream direction as we have observed in Figure 9, but it regains some strength at the large downstream angle around 160° . However, this downstream screech intensity is not obvious in the OASPL contours shown in Figure 10.

B. Frequency and Wavenumber Analysis

Frequency-wavenumber Fourier analysis is employed to compute the wave characteristics of pressure waves in the near field along the conical surface shown in Figure 2(a). Pressure waves along the conical surface are transformed into the frequency-wavenumber space as shown in Figure 14. Since the conical surface used here is 9.5° to the jet axis, the upstream direction is upstream of 80.5° , rather than 90° . The number of bins in the frequency direction is 4096 and 512 in the wavenumber direction. There are actual 271 points along the conical surface, and those points are placed in the middle region of 512 bins and zero padding is applied to the remaining portion. In addition, a window function based on hyperbolic tangent functions is applied to the two ends of the data on the conical surface to reduce the spectral leakage. Azimuthal averaging is used to further smooth the data. In each figure, the dash lines are the propagation paths where pressure waves travel at the ambient sound speed, and thus the supersonic phase speed region (in reference to the ambient sound speed) is between these dash lines. The phase speed is defined as $2\pi f/k$, where f is the frequency and k is the wavenumber along the direction of 9.5° to the jet axis. It can be seen that the dominant portion of the pressure wave intensity on the conical surface is in the supersonic phase speed region. However, a small subsonic phase speed region is observed near the origin of coordinates. It indicates that the current FW-H surface is not completely free from the subsonic traveling waves. But this subsonic portion is small and is limited to very large scales at low frequencies.

The screech tones are more visible in the frequency and wavenumber space. In the cold overexpanded jet, the fundamental screech tone has its signature in both upstream and downstream directions and even in the subsonic propagating region. The second harmonic tone is found near the frequency axis, indicating that this screech harmonic tone has a large phase velocity and its radiation direction should be close to the sideline direction. This is what we have observed in Figure 10. In addition, the third harmonic tone is found in both upstream and downstream directions. A higher harmonic is also observed in Figure 14(a) but its intensity is much weaker. The shock-associated broadband component in the upstream direction is in a lower frequency range than that in the downstream direction. Increasing the jet temperature reduces screech activities and also the upstream intensities, but it greatly increases the downstream propagation intensities, as shown in the high-intensity narrow beams near the dash line. These high-intensity narrow beams should be associated with the Mach wave radiation. As the jet temperature increases, the high-intensity narrow beam broadens and its center moves to a higher phase velocity region. Pressure waves along the lip line are also transformed into the frequency-wavenumber space, as shown in Figure 15. But no azimuthal averaging is used in these figures, so contours do not look as smooth as those shown in Figure 14. The downstream propagating waves clearly dominate pressure waves along the lip line. In addition, high frequency activities are found much more in the downstream direction than in the upstream direction, and the upstream intensity is concentrated mainly in high-intensity harmonic tones. The

supersonic portion (referred to the ambient sound speed) in the cold jets is only a small portion of the total energy, but the radiating portion increases with the jet temperature.

Figure 16 shows the overall pressure intensity versus the acoustic Mach number M_a along both the conical surface and the lip line. The acoustic Mach number M_a is the ratio between the phase velocity (or also referred as the convection velocity) U_c and the ambient sound speed a_{amb} . The total pressure wave energy inside a given range of $[M_a - \frac{1}{2}\Delta M_a, M_a + \frac{1}{2}\Delta M_a]$ is first computed. The pressure intensity at M_a is then computed by divided that total wave energy with ΔM_a . In this paper, $\Delta M_a = 0.05$ is used. It should be mentioned that the acoustic Mach number M_a shown in Figure 16(a) is in reference to the direction of 9.5° to the jet axis. It would be slightly different from its counterpart in the jet axis direction. If the phase velocity is supersonic, the axial counterpart can be computed as $1/\cos(\pi - \cos^{-1}(1/M_a) - 9.5^\circ)$ by using the wavy wall analogy. It can be seen that most of the energy is in the supersonic propagation region along the conical surface, but there is a small portion falling into the subsonic propagation region as we have observed in Figure 14. The percentage of the supersonic portion to the total energy on the conical surface is 0.73, 0.94 and 0.96 at $TTR = 1.0, 2.0$ and 3.0 , respectively, but it is 0.16, 0.41 and 0.56 on the lip line. The subsonic portion in the cold jet on the conical surface is not negligible, but as we have observed in Figure 14, the subsonic portion is found mainly in very large scales at low frequencies. In addition, the supersonic peak level shown in Figure 16(a) increases substantially when the temperature is increased from $TTR = 1.0$ to $TTR = 2.0$, but the increase slows down as the jet temperature further increases. On the other hand, the peak along the lip line is less sensitive to the change of the temperature and it decreases slightly as the jet temperature increases in the overexpanded jets. However, peak intensities along the lip line in shock-free jets remain almost the same. This indicates that the small reduction of the lip-line peak intensities in overexpanded jets probably is caused by the reduction of the downstream screech intensity. A similar trend is found in the overall fluctuation energy that the supersonic portion increases substantially with the jet temperature, but the change of the subsonic portion is very small. It appears that the increase of the pressure wave energy due to the increase of the jet temperature mainly goes into the supersonic portion. Furthermore, the peak acoustic Mach numbers along the lip line are around 0.80, 0.87 and 1.0 at $TTR = 1.0, 2.0$ and 3.0 , respectively. It can be seen that along the lip line, only the jet at $TTR = 3.0$ has a peak phase velocity comparable to the ambient sound speed. In addition, the profile near the peak location broadens and extends further into supersonic phase velocity region, which produces a long supersonic tail. This long supersonic tail is also observed in wavenumber spectra associated with nonlinear wave interaction in Ref. [51]. Peak radiation angles computed from the peak phase velocities shown in Figure 16(a) are 152.8° , 141.0° and 128.3° at $TTR = 1.0, 2.0$ and 3.0 , respectively. These numbers agree well with the peak radiation angles shown in the far-field OASPL distributions in both Figure 10 and Figure 11. This shows that pressure intensities around peak levels shown in Figure 16(a) is associated with the Mach wave radiation.

To examine the radiation direction of pressure waves traveling on the conical surface, the data shown in Figure 14(a) and Figure 14(c) are transformed into the coordinate system of the frequency and radiation angle using the wavy wall analogy. The results are shown in Figure 17, and Figure 18 shows the far-field SPL contours at $r = 100D$. It can be seen that there is a strong similarity between the near- and far-field peak radiation directions, for example, the radiation direction of the fundamental screech tone and its harmonics, the broadband shock-associated peak direction and the peak direction of the mixing component. However, there are some differences in the relative magnitudes, for example, the difference in the rapid increase of the shock-associated broadband frequency between 120° and 130° , where this rapid increase in the far-field distribution is more visible than that in the near-field distribution. In addition, there are also some differences in the middle- to high-frequency ranges near the peak radiation angle around the peak radiation direction. The difference can be seen more clearly in Figure 19(a), where both the near- and far-field results at the 90° and 150° are shown. To have a clearer comparison, an offset

is added to the near-field results to match the far-field peak level at 150° . It can be seen that the far-field results at these two locations present typical large-scale and fine-scale spectra [58], but the near-field profiles show a much weaker high-frequency component in both radiation directions. If we examine the source terms in the FW-H integration equation [49], we can see that the source terms are not only associated with the near-field fluctuations of pressure and velocities, but more importantly they depend on their time derivatives. The following are the magnitude of the dipole source associated with the near-field pressure:

$$p(St, \vec{x}) \cos(\alpha) / r^2 \sqrt{1 + \left(\frac{2\pi St U_j}{a_{amb}} \frac{r}{D} \right)^2}, \quad (1)$$

where α is the angle between the surface normal and the radiation direction, r is the distance between the source and the observer's locations, and $p(St, \vec{x})$ is the near-field pressure on the integral surface. The presence of the frequency itself in the source magnitude is introduced by the Fourier transformation of the time derivative terms in the dipole source terms. It can be seen that the source term weights more on high frequencies as the far-field distance increases. Pressure waves initially decrease at a faster rate of r^{-2} , but the decay rate is reduced to r^{-1} when $\frac{r}{D} \gg \frac{a_{amb}}{2\pi St U_j}$. In addition, high frequencies will reach the decay rate of r^{-1} sooner. For example, the required distance to reach the decay rate of r^{-1} in the cold jets would be $r \gg 0.13D$ at $St = 1.0$ but $r \gg 1.3D$ at $St = 0.1$. In addition, the monopole source term is also a time derivative associated with the surface normal flux. It is clear that time derivatives of the near-field pressure and velocity fluctuations, rather than the fluctuations themselves, are more important to the far-field noise intensity. Thus far-field noise profiles will present higher levels of high frequencies than that in the near field, and this is what we have observed in Figure 19(a). This also explains why the rapid increase of the shock-associated broadband frequency between 120° and 130° in the far field is much larger than that in the near-field distribution. We have found in Ref. [18] that the location of this rapid increase has the maximum level of the shock-associated broadband noise in jets at an underexpanded condition. It is clear that this rapid increase of the shock-associated broadband frequency shown in Figure 18 is responsible for the small peak shown between 120° and 130° in the far-field noise contours in Figure 10(a). Furthermore, the intensity at the screech frequency in the near field is compared with that in the far field as shown in Figure 19(b). It can be seen that the near- and far-field trend is very similar. The screech intensity is high at radiation angles close to the jet axis in both upstream and downstream direction, but the weakest intensity is found between 100° to 140° . In addition, the downstream propagating screech tone has a lower intensity than that in the upstream direction.

Since the conical surface is located close to the jet plume, the distribution of the pressure wave intensity on that surface can provide some insights on the strength of the noise source in the jet plume. Figure 20 shows intensities of pressure waves propagating upstream of 80.5° and intensities of the downstream propagating waves associated with Mach wave radiation on the conical surface. The total intensities are also presented. The downstream propagating waves are between 143° and 162° in the cold jet, between 128° and 150° in the heated jet of $TTR = 2.0$, and between 120° and 141° in the heated jet of $TTR = 3.0$, respectively. The peak radiation angles shown in Figure 10 are 152.8° , 138.9° , and 129.6° at these three jet temperatures. It can be seen that these ranges are large enough to include the dominant portion of the Mach wave radiation. As a whole, the dominant intensity of the upstream propagation waves propagating on the conical surface resides upstream of $10D$ at all three jet temperatures. The peak total intensity and the peak upstream propagating intensity in the cold jet is found near the nozzle exit because of the large contribution from the screech tone. In addition, the intensity associated with Mach wave radiation reaches a substantial level at $x = 5D$. In the two heated jets, however, both the total peak intensity and the intensity contributed by the Mach wave radiation reach substantial levels at $x = 2D \sim 3D$, and this location appears to move closer to the nozzle exit as the jet temperature increases.

Since the surface radius of the conical surface varies in the axial direction, the pressure wave intensity on the conical surface is impacted by the surface radius variation. Thus, the pressure wave intensity itself is not sufficient to measure the relative source strength. Figure 21 shows the radial profiles of $20\text{Log}_{10}(\frac{p'}{p_{ref}} \cdot \frac{r}{D})$ at multiple axial locations. It can be seen that the conical surface is located in the region where the pressure intensity p' decays at r^{-1} . Thus, it would be expected that the production of $p' \cdot r$ on the conical surface dictates the far-field noise strength. Figure 22 shows the axial distributions of $20\text{Log}_{10}(\frac{p'}{p_{ref}} \cdot \frac{r}{D})$ on the conical surface. It can be seen that a substantial level associated with the Mach wave radiation extends to a large axial distance in all three jets. In the cold jet, the production $p' \cdot r$ associated with Mach wave radiation presents a substantial level at $x = 5D$, but it gradually increases further downstream and reaches a broad peak level near $x = 20D$. On the other hand, the peak level of the production $p' \cdot r$ is found near the end of the jet core in these two heated jets. The peak level contributed by upstream propagating waves is also found near the end of the jet core in these two heated jets, but upstream peaks are more conspicuous than those associated with the Mach wave radiation. To visually examine noise source distributions, pressure waves associated with Mach wave radiation are extracted from the pressure fluctuations in the jet plume. The results are shown in Figure 23, where pressure fluctuations that include contributions from all frequencies and wavenumbers are also presented for comparison. It can be seen that the similarity of these two types of distributions increases as the jet temperature increases, because the Mach wave radiation becomes a more important mechanism in the noise generation in heated jets. It can be also seen that Mach wave radiation is closely related to instability waves originated in the shear layer. It appears that smaller scales near the nozzle exit in the shear layer produce Mach wave radiation with small wavelengths, but large scales in more downstream locations produce Mach wave radiation with larger wavelengths.

Figure 24 shows the near-field frequency dependences of the peak phase velocity, the corresponding radiation angle and the peak intensities. The peak intensity at a given frequency is the intensity of the wavenumber that has the maximum intensity at that frequency. The peak phase velocity at that frequency is the phase velocity of the wavenumber that has the maximum intensity. The Pressure waves propagating between 80.5° and 170.5° are presented, and the phase velocity is the axial wave speed. It should be mentioned that since the radiation direction is computed from the phase velocity based on the wavy wall analogy, the peak phase velocities of waves radiate at 90° could be infinite. In the cold jet, the peak phase velocity initially increases with frequency and reaches the maximum value around $St = 0.2$, after which the peak phase velocity decreases with the frequency up to $St \sim 2.5$. The peak phase velocity is greater than $0.8U_j$, and the maximum peak phase velocity near $St = 0.2$ is $0.95U_j$. The peak intensity at the frequency near $St = 0.2$ radiates in the peak radiation direction, but the peak intensities at other frequencies radiate in slightly more downstream radiation directions. In the frequency range higher than $St > 2.5$, the peak phase velocity increases quickly and the radiation angle decreases from 165° to 120° . If we examine the near-field SPL contours of pressure waves in **Figure 25**, the contribution of Mach wave radiation, which is in the region where the acoustic Mach number is slightly greater than one, gradually disappears in the frequency range above $St = 2.5$. The frequency at the radiation angle of 120° is near the resolved frequency ($St \sim 4.0$) in the cold jet simulations. Thus, the radiation direction of higher frequencies where Mach wave radiation is not an important noise generation mechanism shift more upstream and extends to a large range of radiation directions. In addition, since the radiation direction in these distributions is from 80.5° to 170.5° , rather than from 90° to 180° , negative phase velocities are also observed and those negative values correspond to radiation direction upstream of 90° . The large magnitudes of the phase velocities at $St = 0.61$ are associated with the second screech harmonic tone radiating near 90° . In addition, the radiation direction of the peak screech intensity is observed near 160° , which is associated with the downstream propagating screech tone. It is worth noting that the peak phase velocity distribution in the cold jet, not including the impact of the screech harmonics, show a close resemblance to the convection velocity distribution of a supersonic jet at $M_j = 2.1$ presented in Ref. [42].

The convection velocity in that paper was computed by using a vortex sheet model and the convection velocity distribution was found to agree well with measurement data.

The near-field distributions of the heated jets are very different from the cold jet distributions. In these heated jets, the peak phase velocity ratio U_c/U_j is lower than that of the cold jet and the maximum phase velocity is near $0.78U_j$. The Strouhal number associated with the maximum phase velocity is much higher and is near $St = 1.5$. In addition, the dominance of the Mach wave radiation extends to a larger Strouhal number to $St \sim 3.0$. It should be mentioned that since the data were stored at an axial spatial resolution of $0.1D$ on the conical surface, the normalized wave number that can be resolved by this spatial resolution is $k \cdot D$ is 31. This wave number range may not be able to cover the entire frequency range that Mach wave radiation dominates. Thus, the dominance of Mach wave radiation may have extended to a Strouhal number larger than 3.0 in these heated jets, especially in the jet of $TTR = 3.0$. This can be seen in in Figure 14. However, based on what we have obtained from the current heated jet simulations, it appears that the peak phase velocity distributions can be divided into three regions. The first region is in a very low-frequency range below $St = 0.1$. Frequencies in this region radiate at very large downstream angles. The second region is roughly between $St = 0.1 \sim 0.3$, where the radiation direction is slightly downstream of the far-field peak radiation direction. The third region is between $St = 0.3 \sim 3.0$, where the radiation direction is very close to the Mach wave radiation direction. It is clear that, Mach wave radiation is not limited to one frequency or one scale; rather, it is an integrated impact over a large frequency range in heated jets. Furthermore, large peak intensities are found in low frequency range around $St = 0.2$ in both cold and heated jets. It is clear that in heated jets, the dominant waves in low frequency range radiate at directions slightly downstream of the peak radiation direction. This indicates that low frequencies that radiate in the peak radiation direction have larger wavelengths and lower intensities than those dominant low-frequency waves.

Figure 26 shows the peak phase velocities along the lip line. It can be seen that distributions at these three jet temperatures show a similar trend that the peak phase velocity increases with the frequency, but the increase slows down above $St = 0.3$. The peak phase velocity in the cold jet is smaller than the ambient sound speed because hydrodynamic pressure waves dominate. Because the peak phase velocity is lower on the lip line, the resolved maximum wavenumber $k \cdot D = 31$ covers even smaller frequency range than that on the conical surface. The resolved Strouhal number is up to $St \sim 3.0$ in the cold jet, as shown in Figure 15. Thus the peak frequency in the higher-frequency range is not presented in Figure 26. It can be seen that the peak phase velocity distribution along the lip line is very different from that on the near-field conical surface in the cold jet. This is because the lip line is dominated by hydrodynamic pressure waves but the conical surface is dominated by radiating pressure waves. On the other hand, the peak phase velocity distributions in the heated jets along the lip line are more similar to those shown on the conical surface. This is probably because the portion of the radiating pressure waves along the lip line increases with the jet temperature, and the correlation between the pressure fluctuations along the lip line and the radiating pressure waves in the near field is thus higher.

C. Noise Characteristics in Azimuthal and Axial Space

Figure 27 shows pressure fluctuation intensities of five azimuthal modes at three near-field locations on the conical surface in the overexpanded cold jet. It can be seen that the local low-frequency mixing peak at $St \sim 0.2$ at the location above the nozzle exit in Figure 27(a) is contributed by the axisymmetric mode $m = 0$. This axisymmetric mode is also the major contributor to the low-frequency peak of a downstream location at $x = 20D$ as shown in Figure 27(c). This suggests that the frequency component around $St = 0.2$ has a substantial intensity and it propagates in both upstream and downstream directions. On the other hand, the fundamental screech tone at $St = 0.305$ is mainly contributed by the mode of $m = 1$. This shows that the screech tone at the jet Mach number of 1.47 is in a helical mode, which is consistent with the result shown in Refs [9] and [29]. In addition, the screech tone also impacts other higher modes. The

second harmonic tone at $St = 0.61$ is largely contributed by two azimuthal modes, $m = 0$ and $m = 2$, and this can be seen very clearly at its peak location of $x = 7D$, as shown in Figure 27(b). In addition, the mode $m = 1$ is the major contributor to low frequencies below $St = 0.1$ at the location where the screech intensity is high, whereas the mode $m = 0$ is the major contributor to low frequencies at the location where the screech intensity is much weaker. Figure 28 shows the dependence of the overall pressure wave intensities on the acoustic Mach number and also on the radiation direction for the first four azimuthal modes in the cold overexpanded jet. The data are taken from the conical surface. Only pressure waves propagating downstream of 80.5° are included in the study of the dependence on the acoustic Mach number. The magnitudes of higher modes are small, so they are not shown in these plots. Since this analysis is conducted along the conical surface, the computed phase velocity is infinite at 80.5° , so the information near 80.5° is not presented in Figure 28(b). The oscillations shown in the direction close to 80.5° are probably associated with the choice of the resolution of the acoustic Mach number in these calculations. It can be seen that the downstream overall peak intensity is dominated by the axisymmetric mode. Since the downstream overall peak intensity is dominated by the Mach wave radiation, it is clear that Mach wave radiation is dominated by the axisymmetric mode. The far upstream direction, however, is dominated by the helical mode because of the strong presence of the screech tone. On the other hand, the mode dependence is much less in the direction around the sideline between 70° and 110° . It can be also seen that the radiation directions of higher modes are much less directional.

Figure 29 shows the axial dependence of azimuthal intensities on the conical surface in the cold jets. In the shock-free jet, the azimuthal intensities of the production $p'_m \cdot r$ (m is the azimuthal mode number) grow at a similar rate in the axial direction before they reach their peak levels. Higher modes reach their peak levels earlier, and thus their peak levels are lower and the peak levels occur more upstream. The mode $m = 2$ has a broad peak centered on $x = 10D$, and the mode $m = 1$ also has a broad peak which extends from $x = 10D$ to almost $x = 15D$. The axisymmetric mode reaches the peak level at a further downstream location near $x = 14D$. When shock cells are present and high screech tones are observed, large differences are found in the azimuthal intensity distributions. In the overexpanded cold jet the mode $m = 1$ completely dominates the region near the nozzle exit and it contains more than 95% spectral energy in that area. On the other hand, mode $m = 0$ and $m = 2$ peak near $x = 7D$, and this peak is caused by the second screech harmonic tone, as shown in Figure 27. In addition, the axisymmetric mode dominates the noise intensities downstream of $x = 10D$ in both the overexpanded and shock-free jets, but the ratio between its intensity to the total intensity is lower in the overexpanded cold jet. Figure 30 shows the impact of shock cells and the heating effect on the azimuthal modes. It can be seen that shock cells increase the pressure wave intensities in azimuthal modes upstream of $x = 10D$, and the screech tone and its harmonics have greatly amplified this increase. It is clear that the most elevated mode is $m = 1$ except at the location where the second harmonic tone dominates. Increasing the jet temperature reduces the screech intensity, but it increases the pressure wave intensity over a large range of modes upstream of $x = 5D$. Further downstream, the major impact of the heating effect is found in the first two modes.

D. Noise Sources of Screech Tones

Figure 31 shows the instantaneous pressure fluctuations and also the wave intensities at both the screech and the second screech harmonic frequencies. The upstream propagating pressure fluctuations are also included. It can be seen that large pressure fluctuations bulbs are found in the region roughly from $x = 4D$ to $10D$. It is clear that those high-intensity pressure waves are in a helical mode. The dominant upstream propagating waves reside in the region upstream of roughly $10D$. The origin of the second screech harmonic tone appears to be around $x = 9D$ on the jet axis, but the intensity contours show that the region between $x = 6D$ and $9D$ have significant contribution to the generation of this screech harmonic tone. It can be also seen that the radiation direction of this second harmonic tone is slightly upstream. The intensity contours at the fundamental screech frequency show a highly oscillating pattern and this oscillating wave pattern was referred as standing waves in Refs [22] and [28]. The partial interference

between upstream propagating and downstream propagating waves was considered as the cause of those standing waves as suggested in Ref. [28]. The intensity of the interaction between two waves at the same frequency but traveling at an opposite direction at wavenumbers k_1 and k_2 can be described in the following equation:

$$\|A(x)e^{i(k_1x)} + B(x)e^{i(-k_2x)}\| = A(x)^2 + B(x)^2 + 2A(x)B(x)\cos[(k_1 + k_2)x] \quad (2)$$

A similar formulation can also be found Ref. [28]. It can be seen that if the ratio between these two wave intensities $A(x)/B(x)$ is not small, assuming $A(x) \geq B(x)$, the third term in Eq. (2) will be visible and an oscillating pattern is expected to appear. This is what we have observed in the screech intensity distribution shown in **Figure 31(c)**. The screech intensity is separated into the upstream and downstream propagating portions as shown in **Figure 32**, and the lip-line results are plotted in **Figure 33**. It can be seen that the oscillating pattern is observed upstream of $x = 10D$. The upstream propagating intensity is very small downstream of this location, so the oscillating pattern is not visible. The downstream propagating waves have a broad peak level extending from $x = 3D$ to $7D$, but the upstream peak level is found around $x = 6D$, which is near the 6th shock-cell tip, as shown in **Figure 34**. It is clear that the upstream propagating intensity dominates the total peak intensity, and the axial locations of the local peak intensities are found near the axial locations of shock-cell tips. This is consistent with experimental observations and speculations that shock-cell tips are important noise sources [9].

The peak acoustic Mach number and the peak length scale at the screech frequency are examined in **Figure 35**. The maximum upstream propagating intensity is found below the lip line at $0.3D$ above the jet axis, but the maximum downstream intensity is found near the lip line. Both the dominant upstream and downstream propagating waves travel at a similar acoustic Mach number of $M_a \sim 0.84$ in the jet plume, and this phase velocity is roughly $0.69U_j$. The peak phase velocity increases in the radial direction and reaches a value slightly larger than the ambient sound speed. The peak length scales are also similar in both upstream and downstream directions. In the jet plume, they are roughly $2.2D$, which is 1.76 times the largest shock-cell size. Outside the jet plume they increase to a value near $2.9D$, which should be the dominant length scale of the screech tone. This can be also seen in **Figure 31(c)** where the length scale of the oscillating pattern in the jet plume is indeed smaller than that outside the jet plume. In addition, it can be seen that the upstream propagating screech tone spreads over a large range of wavenumbers, but downstream propagating screech tone is observed in a much smaller wavenumber range. This shows that the upstream propagating screech tones should be more visible than the downstream propagating screech tones. Furthermore, downstream of $x = 4D$, the standing wave fronts extend outside the jet plume, but upstream of $x = 4D$, the standing waves in the jet plume are different from those outside. It appears that standing waves outside the jet plume near the nozzle exit are originated from the region downstream of $x = 4D$.

The shock-cell coherent oscillatory motion was observed in several measurements of highly screeching jets, such as those reported in Refs [23]-[25]. The shock-cell coherent oscillatory motion was considered important to the screech tone generation [23]. Instantaneous pressure fluctuations show that downstream shock cells move up and down and also rotate. Shock cells show distinctively different orientations near the upper/lower lip lines and the jet axis. **Figure 36** shows three instantaneous shock-cell oscillation patterns to highlight the three phases of shock-cell oscillations, which are very visible in the 4th, 5th and 6th shock cells. It can be seen that the downstream shock cells tilt towards downstream when they move to the upper half of the jet core and tilt towards upstream when they move to the lower half. On the other hand, shock cells show the least rotation when they are near the jet axis. A very similar pattern has also been observed in an underexpanded screeching jet of $M_j = 1.4$ in Ref. [24], where the time-averaged and phase-averaged data were obtained by a narrow laser beam traversed from point to point in the flow field and the appearance of the scattered light was sensed by a photomultiplier tube. It was observed in **Figure 9** of that paper that the upper half of the shock conical boundary is absent when the lower half is the

strongest, while the lower half is absent when the upper half is the strongest. This observation clearly agrees with the shock-cell oscillation patterns shown in Figure 36. The shock conical boundary reported in Ref. [24] also shows a similar alignment to the jet axis as the shock alignment shown in Figure 36. Further examination of instantaneous pressure fluctuations shows that shock cells rotate in a counterclockwise direction when they move down near the lower lip line and interact with passing pressure waves. When they move up, they rotate in a clockwise direction and also interact with pressure waves near the lip line before they move back to the jet axis. They continue to move up near the upper lip line and interact with pressure waves there. Afterwards, they move down again and rotate in a counterclockwise direction until they reach the lower lip line. This process repeats itself, and neighboring shock cells are found move and rotate in an opposite direction. It is clear that the shock-cell coherent oscillatory motion, especially the shock-cell rotation, is caused by the upstream and downstream propagating waves. The downstream propagating waves should be initiated from the shear layer near the nozzle exit. When instability waves interact with shock cells, shock cells oscillate and in turn generate additional upstream and downstream propagating waves, which can cause more shock-cell oscillation motion. The increased shock-cell oscillations can generate even stronger upstream and downstream propagating waves until the process reaches to the fully developed status. To examine how pressure waves are generated by the interaction between shock cells and passing waves, a smaller range of intensity contours is used and shown in Figure 37. It can be seen that high-intensity waves are generated when two neighboring shock cells rotate at an opposite direction and appear to “collide” with each other. Similar patterns have also been observed in measurements of Ref. [25]. This collision is the interaction between waves generated by two neighboring shock cells interacting with passing waves. If we examine locations of those high-intensity pressure waves in Figure 34 and Figure 37, it can be seen that they are located between two compression waves and are near the shock-cell tips. It is clear that those high-intensity pressure waves are responsible for the peak intensities located near shock-cell tips at the screech frequency. Thus, the upstream/downstream propagating waves and the induced shock-cell coherent oscillatory motion reinforce each other and form a reinforcing loop in this highly screeching jet.

The magnitude of shock-cell oscillations can be observed in Figure 38, where turbulence intensities at the screech frequency are presented. High-intensity coherent turbulence structures of axial velocity fluctuations are found near the lip line region between $x = 4D$ to $9D$. The radial and the tangential velocities show large coherent fluctuations along the jet axis, and they are in phase with each other. However, the radial intensity is much larger than the tangential intensity. Since shock cells have both radial and tangential velocities, it is very likely that shock cells oscillate in a helical mode similar to that of the screech tone. In addition, the radial intensity also presents a coherent structure near the lip line and this radial intensity along the lip line is found in phase with the lip-line pressure intensity, as shown in Figure 38(d). But they are out of phase with the axial turbulence intensities by roughly 90° . It is worth noting that lines connecting the peak radial intensities at the jet axis and the peak radial intensities along the lip line are very close to the directions of the shock-cell alignment when they reach lip lines as shown in Figure 36. The rotation motion of shock cells appears to be coupled with a small radial motion near lip lines. The largest cross-sectional velocity fluctuation intensity, however, is found near the jet axis. Furthermore, it should be mentioned that the current turbulence intensity distributions show a strong similarity to those observed in the measurement of a screeching axisymmetric jet in the helical C mode [32], where Proper orthogonal decomposition (POD) method was used to separate the coherent structure from the random axial stresses.

When the jet temperature ratio is increased to $TTR = 2$, the level of Mach wave radiation intensity is increased, and the source region of the Mach wave radiation at the screech frequency extends further upstream than that in the cold jet as shown in Figure 39. In addition, the turbulence fluctuation intensities at the screech frequency in this heated jet are shown in Figure 40. It can be seen that the shock-cell oscillation magnitude is substantially reduced and the largest reduction is found in the radial component. The turbulence intensities near the lip-line region also show less coherent patterns. However, the structure

of the radial and tangential intensities at the jet axis still remains coherent. As pointed out in Ref. [21] that since screech tones are powered by the instability waves, the naturally occurring tones must be associated with highly amplified band of instability waves. It was shown in that paper that the increase of the jet temperature increases the difference between screech frequencies and the frequencies of the most amplified instability waves. It was argued in that paper that the energy of the instability waves at the screech frequency would be too low to generate high-intensity screech tones in hot jets. The current LES results in Figure 8 also show that the difference between these two frequencies increases slightly as the jet temperature increases. But the peak intensity at the screech Strouhal number of $St = 0.26$ in the heated jet of $TTR = 2$ is still substantial comparing to the maximum peak intensity, as shown in Figure 24. It was also shown in that paper that the frequency difference between screech tones and the most amplified instability frequency decreases as the jet Mach number increases, and thus, it would be expected that the screech intensity be higher if the jet Mach number is larger. But this conclusion does not align with the observation that screech intensities are often higher in overexpanded jets than in underexpanded jets [54]. Thus, it appears that the frequency match between screech tones and the most amplified instability waves may not be the only factor that is important to the screech generation. As we have discussed in the previous text that in the highly screeching overexpanded cold jet, the upstream and downstream propagating waves and the induced shock-cell coherent oscillatory motion are in a reinforcing loop. To sustain this coherent opposite rotation of neighboring shock cells, dominant upstream and downstream propagating waves should travel at a similar phase velocity. Thus, the match of the peak upstream and downstream propagating phase velocities appears to be another important factor to the generation of the screech tone. Figure 41 shows the lip-line intensities of upstream and downstream propagating waves versus the phase velocities in both the cold overexpanded and shock-free jets and also the heated overexpanded jet at $TTR = 2.0$. It can be seen that only the highly screeching jet has a similar upstream and downstream propagating peak phase velocities. In the heated jet, the downstream peak phase velocity increases, but the upstream peak phase velocity remains almost the same. On the other hand, the shock-free cold jet does not present a clearly defined peak upstream phase velocity at all. This indicates that shock cells are the major source responsible for the dominant upstream propagating waves in these shock-containing jets. Thus, it is not a surprise that the heating effect on the peak upstream propagating phase velocity is small, because the heating effect on the shock-cell structure is small as shown in Figure 3 and Figure 4. The increased phase velocity of downstream propagating waves in heated jets is because instability waves travel at larger convection velocities as the temperature increases. The increased difference between the upstream and downstream peak phase velocities would weaken the reinforcing loop between upstream/downstream propagating waves and the shock-cell oscillatory motion. Thus, this makes the simultaneous opposite rotation of neighboring shock cells less frequently. This would weaken the generation of the high-intensity pressure waves at the screech frequency. Figure 42 shows similar distributions of underexpanded jets reported in Ref. [18]. It can be seen that there is a visible difference between upstream and downstream peak phase velocities even in the cold underexpanded jet. This explains why the screech intensity is weaker in the underexpanded cold jet. In addition, it can be seen that the magnitude of the phase velocity difference varies less with the jet temperature in underexpanded jets because the difference between upstream and downstream peak phase velocities changes sign from the cold jet to the heated jet at $TTR = 2.0$. This may further explain why the heating effect has less impact on the screech intensity in these underexpanded jets. It can be seen that if the high-intensity pressure waves at the screech frequency are weakened, the induced shock-cell oscillatory motion should also be reduced, and this is what we have observed in Figure 40. The phase velocity match between upstream and downstream propagating waves is important to the generation of the screech tone may also explain why the upstream reflection can increase the screech intensity. This is because the downstream propagating waves generated by the reflection of the upstream propagating waves will reduce the difference between the upstream and downstream propagating peak phase velocities and thus increase the shock-cell coherent oscillatory motion and the screech intensity.

IV. CONCLUSIONS

The noise characteristics in overexpanded jets have been investigated by analyzing LES results generated by an unsteady compressible flow solver embedded in JENRE. Three jet temperatures are considered. The overexpanded cold jet is highly screeching, and the fundamental screech tone is in a helical C mode. The impact of the high-intensity screech tone is similar to those observed in the past. For example, it shortens the jet core length, increases the turbulence level and perturbs the low-frequency component. The screech tone is found to propagate in both upstream and downstream directions and the radiation direction of the peak screech intensity is found slightly above the jet axis. The weakest screech intensity, on the other hand, is found downstream of the sideline direction between 100° to 140° . Increasing the jet temperature reduces the screech intensity and eliminates higher screech harmonics at this overexpanded jet condition. However, the screech intensity is not sensitive to the heating effect in mildly screeching underexpanded jets in our previous work [18].

Increasing the jet temperature has greatly increased Mach wave radiation, which dominates the noise generation in the two heated jets. The peak noise level moves upstream as the jet temperature increases. The noise intensity of Mach wave radiation is found in a large axial range in the near field, and a small peak level is observed near the end of the jet core in the two heated jets. The extracted instantaneous fields associated with Mach wave radiation clearly demonstrate that that instability waves originated in the shear layer are the source of Mach wave radiation. As the jet temperature increases, the intensity of hydrodynamic pressure fluctuations remains similar, but the radiating intensity increases substantially. The near-field peak phase velocity profile in the cold jet is very different from those in heated jets. The maximum peak phase velocity ratio U_c/U_j is located at a low frequency near $St = 0.2$ in the cold jet, but it is located at a much higher frequency in heated jets. In addition, the peak phase velocity ratio U_c/U_j has a larger magnitude in the cold jet. The profile of the peak radiation direction in the cold jet presents two distinctively different frequency ranges, one is dominated by Mach wave radiation, and another is in a higher-frequency range where Mach wave radiation does not dominate. In the first frequency range, the peak directions are located mainly in large downstream directions. In the second frequency range, the peak radiation direction has a broader range of radiation angles and moves towards the sideline direction as the frequency increases. In the cold jet, the peak radiation direction near $St = 0.2$ is found align with the far-field peak radiation direction. In the two heated jets, peak frequencies radiating at the far-field peak radiation direction extends to a much larger frequency range between $St \sim 0.3 - 3.0$. The high end of this range is based on the current spatial resolution of the data stored on the conical surface. It is possible that this high end is higher than those given in simulations. In addition, the higher frequency range (the second frequency range) where the Mach wave radiation does not dominate should be in an even higher frequency range, which is not presented in the current results of the heated jets.

The azimuthal dependence of the pressure wave intensities in the near field is also examined. The mixing peak levels are mainly contributed by the axisymmetric mode, but the fundamental screech tone is contributed by the mode $m = 1$. The second screech harmonic, on the other hand, has contributions from two azimuthal modes: $m = 0$ and $m = 2$. The mode $m = 1$ (screech tone) contains around 95% pressure wave energy near the nozzle exit, but the downstream is dominated by the axisymmetric mode. In addition, the peak radiation direction, or say Mach wave radiation, is dominated by the axisymmetric mode. However, the radiation direction around the sideline shows a much weaker azimuthal dependence. Increasing the jet temperature reduces the contribution from the mode $m = 1$ (screech intensity), but it elevates pressure wave intensity in other modes upstream of $x = 5D$. Further downstream, however, the largest heating impact is found in the first two modes.

The second screech harmonic tone appears to radiate at $x = 9D$ in the instantaneous pressure fields in the highly screeching overexpanded cold jet. But the intensity distribution shows that its source region extends from $x = 6D$ to $9D$. The pressure intensity distribution at the screech frequency has a highly

oscillating pattern due to the interaction between upstream and downstream propagating waves. The axial locations of the local peak intensities are found near the axial locations of the shock-cell tips, and the maximum peak intensity is found near the 6th shock-cell tip. It is found that shock cells rotate in both clockwise and counterclockwise directions, and the neighboring shock cells are found rotate in an opposite direction simultaneously in the highly screeching overexpanded cold jet. High-intensity pressure waves are generated when neighboring shock cells are in a close proximity because of the opposite rotation. These high-intensity pressure waves are referred as standing waves in several literatures. It is found that the high-intensity pressure waves are responsible for the peak intensities observed near shock-cell tips. The upstream/downstream propagating waves and the induced shock-cell coherent oscillatory motion reinforce each other and form a reinforcing loop. The match between the peak upstream propagating phase velocity and peak downstream propagating phase velocity should be important to the sustaining of the reinforcing loop and thus to the screech tone generation. This phase velocity match is only found in the highly screeching jet. The heated overexpanded jets and also underexpanded jets reported in [18] all show substantial differences between the peak phase velocities of upstream and downstream propagating waves. Thus, the mismatch between upstream and downstream peak phase velocities should be an important cause contributing to the screech intensity reduction in the heated overexpanded jets, and this may also explain why the screech tone is weaker in the underexpanded cold jet in our previous work. In addition, the importance of the phase velocity match between upstream and downstream propagating waves to the generation of the screech tone may also explain why the upstream reflection can increase the screech intensity.

ACKNOWLEDGEMENTS

This specific research has been sponsored by the Office of Naval Research (ONR) through the NRL 6.1 Computational Physics Task Area. Additional related research has been sponsored by ONR through the Jet Noise Reduction (JNR) Project under the Noise Induced Hearing Loss (NIHL) program. Computing resources have been provided by the DoD High Performance Computing Modernization Program Office.

REFERENCES

- [1]. Harper-Bourne, M., and Fisher, M. J., "The Noise from Shock Waves in Supersonic Jets," AGARD-CP-131, 1973, pp. 1-13.
- [2]. Tanna, H. K., "An Experimental Study of Jet Noise. Part II: Shock Associated Noise," *Journal of Sound and Vibration*, 50(3), 1977, pp. 429-444.
- [3]. Seiner, J. M., and Norum, T. D., "Experiments on Shock Associated Noise of Supersonic Jets," AIAA paper 79-1526, 1979.
- [4]. Seiner, J. M., and Norum, T. D., "Aerodynamic Aspects of Shock Containing Jet Plumes," AIAA paper 80-0965, 1980.
- [5]. Norum, T. D., and Seiner, J. M., "Measurements of Static Pressure and Far Field Acoustics of Shock-containing Supersonic Jets," NASA TM 84521, 1982.
- [6]. Norum, T. D., and Seiner, J. M., "Broadband Shock Noise from Supersonic Jets," *AIAA Journal*, Volume 20, No. 1, 1982, pp. 68-73.
- [7]. Tam, C. K. W., and Tanna, H. K., "Shock Associated Noise of Supersonic Jets from Convergent-Divergent Nozzles," *Journal of Sound and Vibration*, 81(3), 1982, pp. 337-358

- [8]. Seiner, J. M., and Yu, J. C., "Acoustic Near-Field Properties Associated with Broadband Shock Noise," AIAA Journal, Volume 22, No. 9, 1984, pp. 1207-1215
- [9]. Tam, C. K. W., "Jet Noise Generated by Large-Scale Coherent Motion," Aeroacoustics of Flight Vehicles: Theory and Practice, Volume 1: Noise Sources, ed. H. H. Hubbard, NASA RP-1258, 1991, pp. 311-390.
- [10]. Tam, C. K. W., "Broadband Shock-Associated Noise of Moderately Imperfectly Expanded Supersonic Jets," Journal of Sound and Vibration, Vol. 140, No. 1, 1990, pp. 55-71.
- [11]. Veltin, J., "On the Characterization of Noise Sources Supersonic Shock Containing Jets", PhD dissertation, 2005, the Pennsylvania State University.
- [12]. Bridges, J. and Wernet, M., "Turbulence Associated with Broadband Shock Noise in Heated Jets", AIAA-2008-2835
- [13]. Viswanathan, K., Alkislar, M.B., and Czech, M.J., "Characteristics of the Shock Noise Component of Jet Noise", AIAA 2008-2835
- [14]. Kuo, C-W, McLaughlin, D.K., Morris, P., "Effects of supersonic jet conditions on broadband shock-associated noise", AIAA 2011-1032.
- [15]. Andre, B., Castelain, T., and Bailly, C., "Broadband Shock-Associated Noise in Screeching and Non-Screeching Underexpanded Supersonic Jets", AIAA Journal, Vol. 51, No. 3 (2013), pp. 665-673.
- [16]. Savarese, A., P., Jordan, S, Girard, A., Royer, C., Fourment, E., Collin, Y. Gervais, and M., Porta, "Experimental study of shock-cell noise in underexpanded supersonic jets", AIAA 2013-2080
- [17]. Tam, C. K. W., Viswanathan, K., K. K. Ahuja And J. Panda, "The sources of jet noise: experimental evidence", J. Fluid Mech. (2008), vol. 615, pp. 253-292.
- [18]. Liu, J., Kailasanath, K., Heeb, N., Munday, D., Gutmark, E., "Computational study of shock-associated noise characteristics using LES", NRL/MR/6040-14-9560.
- [19]. Liu, J., Corrigan, A., Kailasanath, K., Heeb, N., Gutmark, E., "Numerical Study of Noise Sources Characteristics in An Underexpanded Jet Flow", 20th AIAA Aeroacoustics conference, 16 - 20 June 2014, Atlanta, Georgia.
- [20]. Powell, A., On the mechanism of choked jet noise, Proc. Royal Society of London, Series B, 66, pp. 1039-1056, 1953.
- [21]. Tam, C. K. W., Ahujia, K. and Jones, III, R.R., "Screech tones from free and ducted supersonic jets", AIAA Journal, No. 5 (1994), pp. 917-922.
- [22]. Westley, R. and Woolley, J., "The near field sound pressures of a choked jet when oscillating in the spinning mode", AIAA 75-479.
- [23]. Suda, H., Manning, T. A., Kaji, S., "Transition of Oscillation Modes of Rectangular Supersonic Jet in Screech", AIAA-93-4323.
- [24]. Panda, J., "Shock oscillation in underexpanded screeching jets" Journal of Fluid Mechanics, 1998, Vol. 363, pp. 173-198.
- [25]. Umeda, Y., and Ishii R., "Sound sources of the screech tone radiated from circular under-expanded jet oscillating in the helical mode", the 18th International Congress on Acoustics ICA 2004, Kyoto, Japan
- [26]. Massey, K.C., Ahuja, K., K., Jones, R., R., and Tam, C.K.W., "Screech Tones Of Supersonic Heated Free Jets", AIAA 94-0141.

- [27]. Raman, G., “Advances in Understanding Supersonic Jet Screech: Review and Perspective,” *Progress in Aerospace Sciences*, Vol. 34, No. 1–2, 1998, pp. 45–106.
- [28]. Panda, J., “An Experimental Investigation of Screech Noise Generation,” *Journal of Fluid Mechanics*, 1999, Vol. 378, pp. 71–96.
- [29]. Raman, G., “Supersonic Jet Screech: Half-Century from Powell to the Present,” *Journal of Sound and Vibration*, Vol. 225, No. 3, 1999, pp. 543–571.
- [30]. Henderson, B., “The connection between sound production and jet structure of the supersonic impinging jet,” *J. Acoust. Soc. Am.* 111(2), 735–747 (2002).
- [31]. Tam, C. K. W., Parrish, S.A, and Viswanathan, K., “Harmonics of Jet Screech Tones”, *AIAA journal*, 2014.
- [32]. Edgington-Mitchell, D., Oberleithner, K., Honnery, D.R., and Soria, J., “Coherent structure and sound production in the helical mode of a screeching axisymmetric jet”, *J. Fluid Mech.*, (2014), vol. 748, pp 822-847.
- [33]. Shen H. and Tam, C. K. W., “Numerical Simulation Of The Generation Of Axisymmetric Mode Jet Screech Tones”, *AIAA J.* Vol. 36, No. 10, October 1998.
- [34]. Shen H. and Tam, C. K. W., “Three-Dimensional Numerical Simulation of the Jet Screech Phenomenon”, *AIAA J.*, Vol. 40, No. 1, January 2002.
- [35]. Suzuki, T., Lele, S.K., Shock leakage through an unsteady vortex-laden mixing layer: application to jet screech, *J. Fluid Mech.*, 490, pp. 139-167, 2003.
- [36]. Loh, C.Y., and Hultgren, L.S., “Jet Screech Noise Computation”, *AIAA J.*, Vol. 44, No.5, May 2006.
- [37]. Berland, J., Bogey, C., and Bailly, C., “Large Eddy Simulation Of Screech Tone Generation In A Planar Underexpanded Jet”, *AIAA* 2006-2496
- [38]. Liu, J.; Kailasanath, K.; Ramamurti, R.; Munday, D.; Gutmark, E.; Löhner, R., “Large-Eddy Simulations of a Supersonic Jet and Its Near-Field Acoustic Properties”, *AIAA Journal*, vol. 47, issue 8, pp. 1849-1864.
- [39]. Mitchell, B.E., Lele, S.K., and Moin, P., “Direct Computation Of Mach Wave Radiation In An Axisymmetric Supersonic Jet”, *AIAA J.*, Vol. 35, No., 10, October 1997.
- [40]. Papamoschou, D. & Debiase, M. 2001 Directional suppression of noise from a high-speed jet. *AIAA J.* 39 (3), 380–387.
- [41]. Krothapalli, A., Arakeri, V., and Greska, B., “Mach wave radiation: a review and an extension”, *AIAA* 2003-1200.
- [42]. Tam, C.K., “Mach wave radiation from high-speed jets”, *AIAA journal*, Vol, No., 10, October 2009.
- [43]. Kearney-Fischer, M., Kim, J.-H., and Samimy, M., “A study of Mach wave radiation using active control”,
- [44]. Oertel, H., (1979), Mach wave radiation of heated supersonic jets. In *Mechanics of Sound Generation in Flows* (ed. E. A. Muller), pp. 275–281. Springer
- [45]. Boris, J.P., and Book, D.L., “Flux-corrected Transport I:SHASTA a fluid transport algorithm that works”, *Journal of Computational Physics*, Volume 11. Issue 1. Pages: 38-69 (1973)

- [46]. Löhner, R., Morgan, K., Peraire, J., and Vahdati, M., “Finite element flux-corrected transport (FEM-FCT) for the Euler and Navier- Stokes equations,” *International Journal for Numerical Methods in Fluids*, Vol. 7, No. 10, 1987, pp. 1093–1109.
- [47]. Kuzmin, D., Möller, M., and Garris, M., “Algebraic Flux Correction II: Compressible Flow Problems,” in *Flux-Corrected Transport: Principles, Algorithms, and Applications*, Eds., D. Kuzmin, R. Löhner, and S. Turek, Springer, pp. 193–238., 2012
- [48]. Zalesak, S.T., “Fully multidimensional flux-corrected transport algorithms for fluids”, *Journal of Computational Physics*, Vol. 31, No. 3, 1979, pp. 335–362.
- [49]. Lyrintzis, A., “Surface integral methods in computational aeroacoustics—From the (CFD) near-field to the (Acoustic) far-field”, *International Journal of Aeroacoustics*, Volume 2, Number 2 / April 2003, pp. 95-128
- [50]. Tinney, C.E. and Jordan, P., “The near pressure field of co-axial subsonic jets”, *Journal of Fluid Mechanics*, 611 (2008)175–204.
- [51]. Suponitsky, V., Sandham, N.D., Morfey, C.L., Linear and nonlinear mechanisms of sound radiation by instability waves in subsonic jets, *Journal of Fluid Mechanics*, 658 (2010)509–538.
- [52]. Ryu, J., Lele, S.K., and Viswanathan, “Study of supersonic wave components in high-speed turbulent jets using an LES database”, *Journal of Sound and Vibration* 333 (2014) 6900-6923.
- [53]. Crawley, M. and Samimy, M., “Decomposition of the Near-Field Pressure in an Excited Subsonic Jet”, AIAA 2014-2342.
- [54]. Munday, D., Gutmark. E., Liu, J., and Kailasanath, K. (2011), Flow structure and acoustics of supersonic jets from conic convergent-divergent nozzles, *Physics of Fluids*, Vol. 23, No. 11, Nov 2011, pp. 116102-1 - 116102-13.
- [55]. Liu, J.; Kailasanath, K.; Heeb, N, Munday, D.; E., Gutmark; Effect of Nozzle-exit Flow Conditions on the Flow and Acoustic Properties of Imperfectly Expanded Supersonic Jets”, AIAA-2012-2061.
- [56]. Panda, J., Seasholtz, R.G., and Elam, K.A., Investigation of noise sources in high speed jets via correlation Measurements, *J. Fluid Mech.* (2005), vol. 537, pp. 349-385.
- [57]. Tam, C.K.W., Pastouchenko, N., and Viswanathan, K., “Fine-Scale Turbulence Noise From Hot Jets”, AIAA journal, Vol. 43, No., 8, August 2005.
- [58]. Tam, C.K.W., Viswanathan, K., Ahuja, K.K., and Panda, J., “The source of jet noise: experimental evidence”, *J. Fluid Mech.*, (2008), vol. 615, pp., 253-292.
- [59]. Tam, C.K.W., Golebiowski, M., and Seiner, J.M., “On The Two Components Of Turbulence Mixing Noise From Supersonic Jets”, AIAA 96-1716.

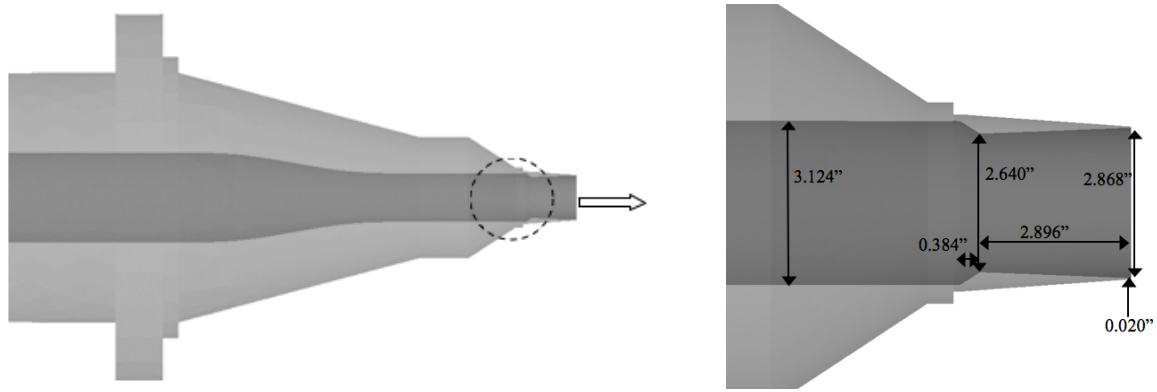


Figure 1. Nozzle geometry. The figure on the right is an enlarged version of the area near the nozzle throat and the exit.

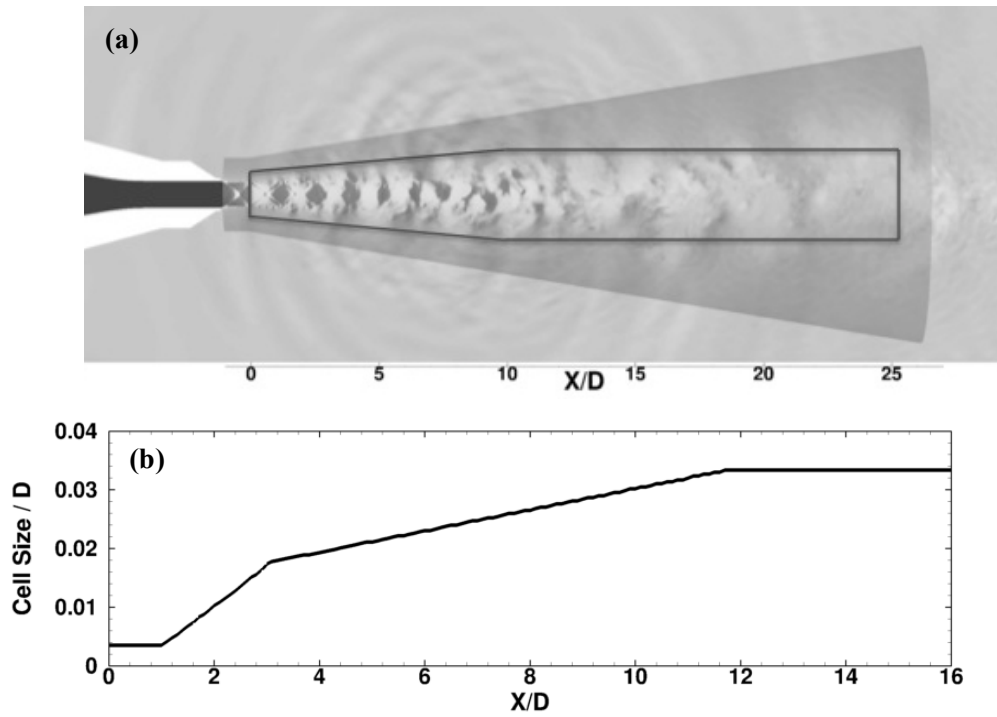


Figure 2. (a). Computational domain. The data on the outer conical surface are used for the far-field noise prediction and also in the frequency-wavenumber analysis. (b). Axial cell size distribution along the lip line.

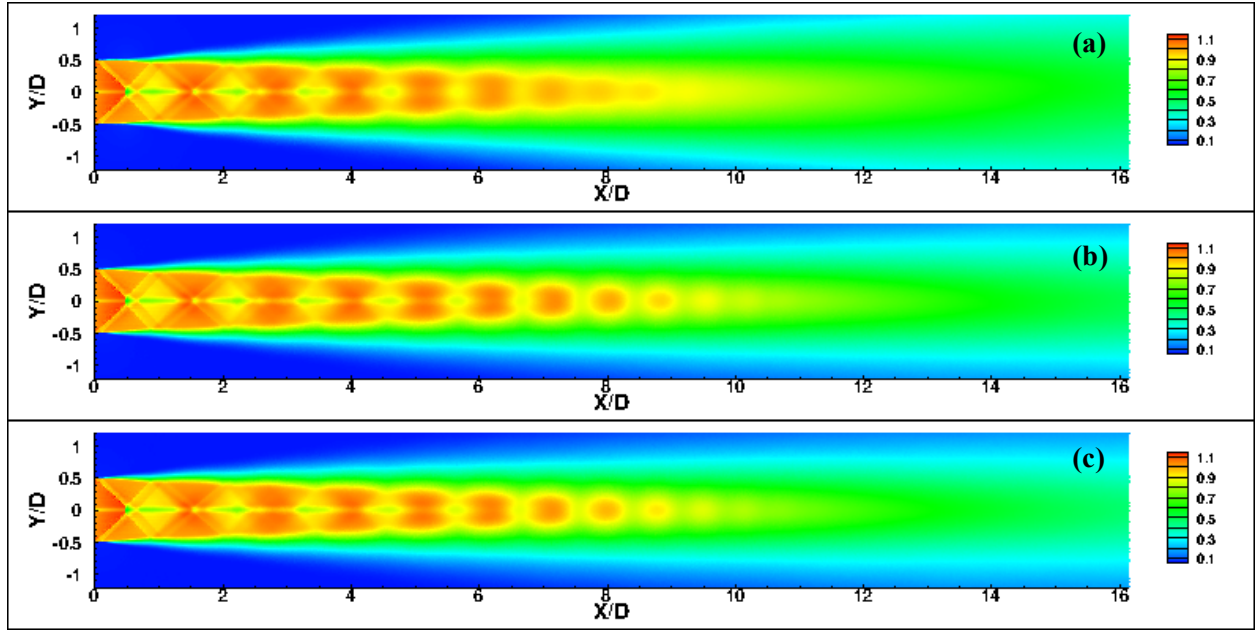


Figure 3. Axial velocity distributions. (a). $TTR = 1.0$. (b). $TTR = 2.0$. (c). $TTR = 3.0$.

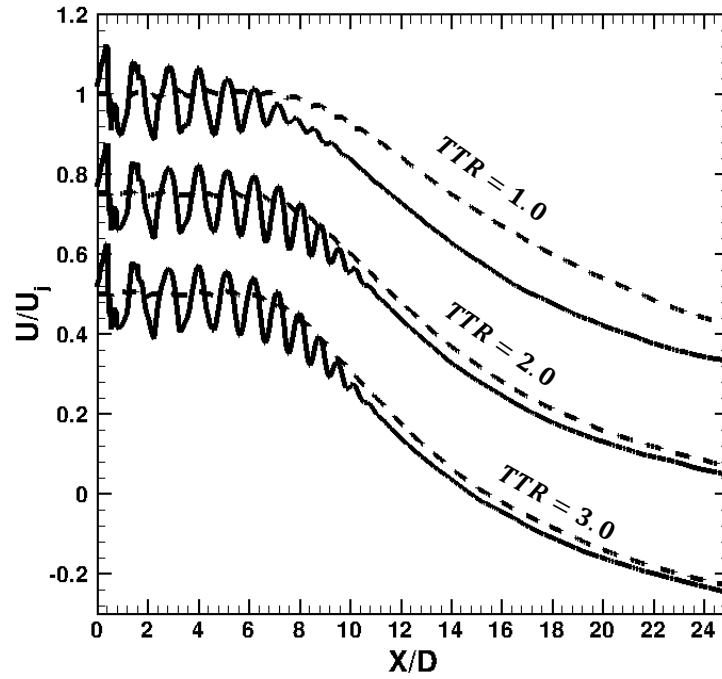


Figure 4. Centerline axial velocity distributions. Solid lines: overexpanded jet. Dashed lines: shock-free jet. The plotted U/U_j is subtracted by $0.25*(TTR - 1)$

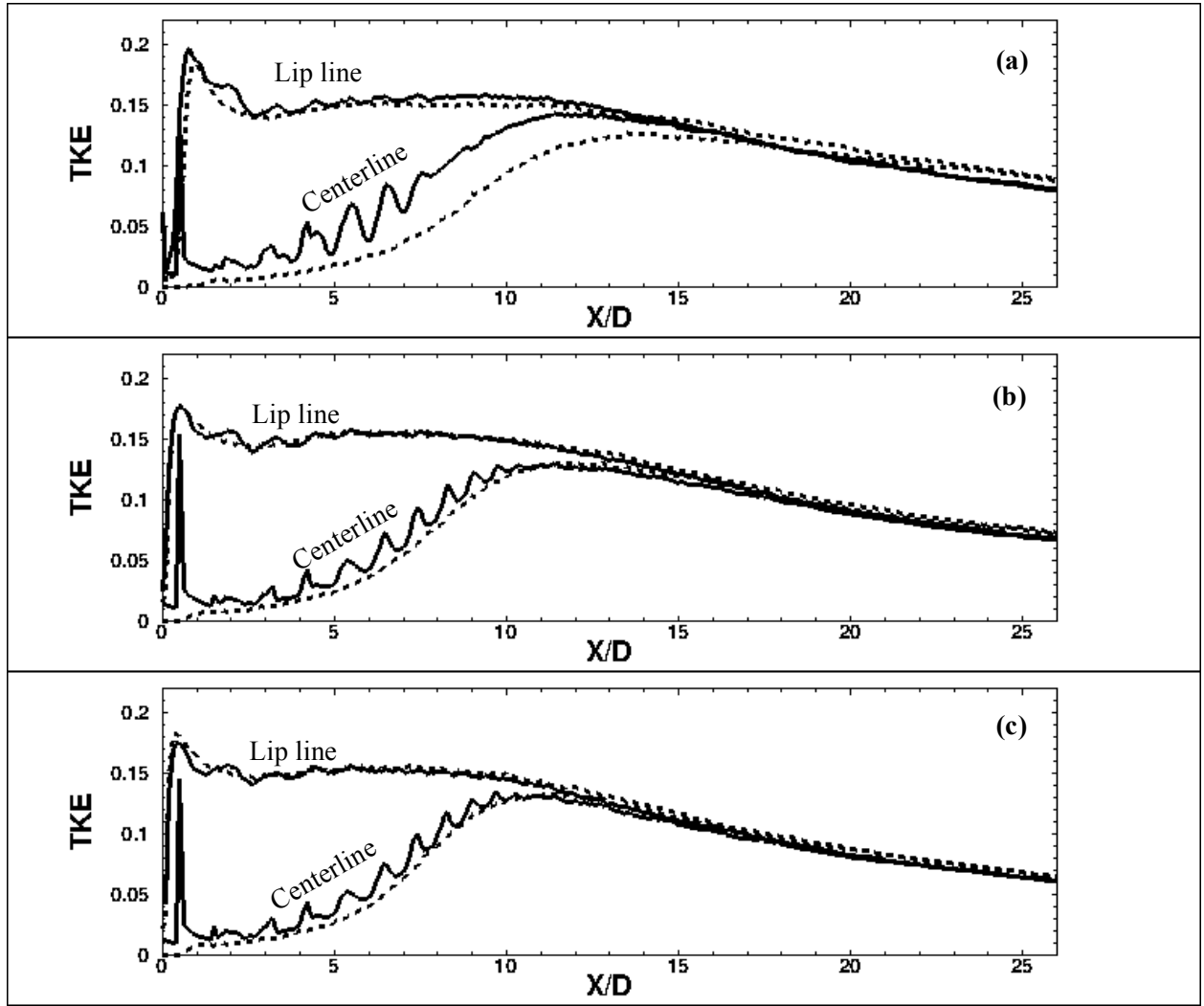


Figure 5. Turbulence kinetic energy along both the centerline and the lip line in the overexpanded and the shock free jets. Solid lines: overexpanded jets. Dashed lines: shock-free jets. (a). $TTR = 1.0$. (b). $TTR = 2.0$. c). $TTR = 3.0$.

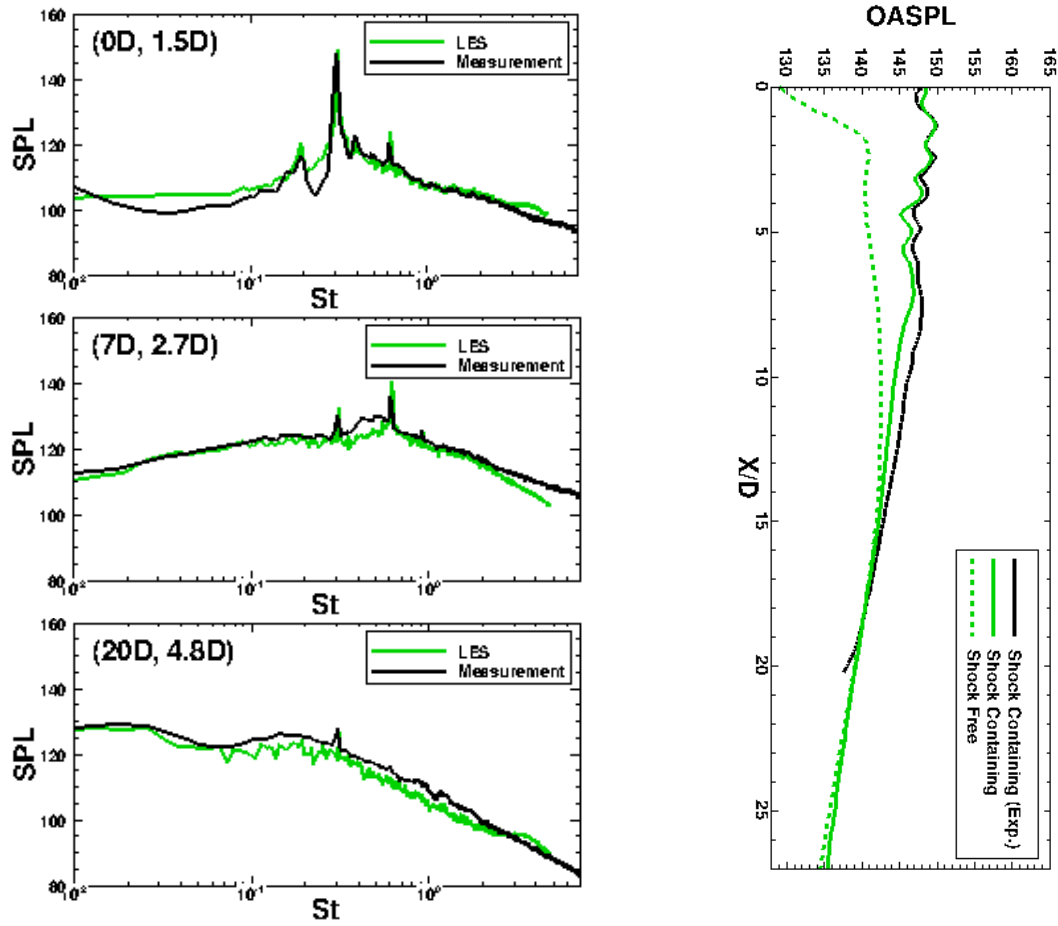


Figure 6. Figures on the left are spectral distributions of the near field sound pressure levels (SPL) between LES predictions and measurement data. The axial and radial coordinates of the location are shown in each figure on the left. Figure on the right shows the overall sound pressure levels along the FW-H surface.

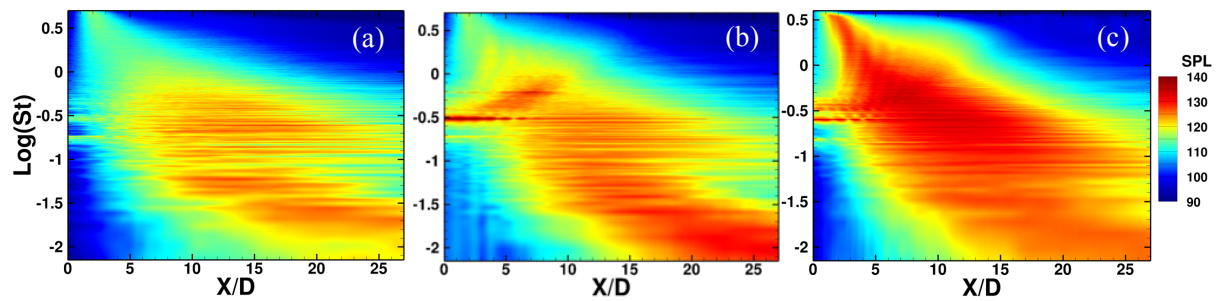


Figure 7. SPL contours along FW-H integral surface. The Strouhal number is plotted in the logarithmic scale to highlight the low-frequency components. (a). The shock-free jet flow at the cold jet condition $TTR = 1.0$. (b). The overexpanded jet flow at $TTR = 1.0$. (c). The overexpanded jet flow at $TTR = 2.0$.

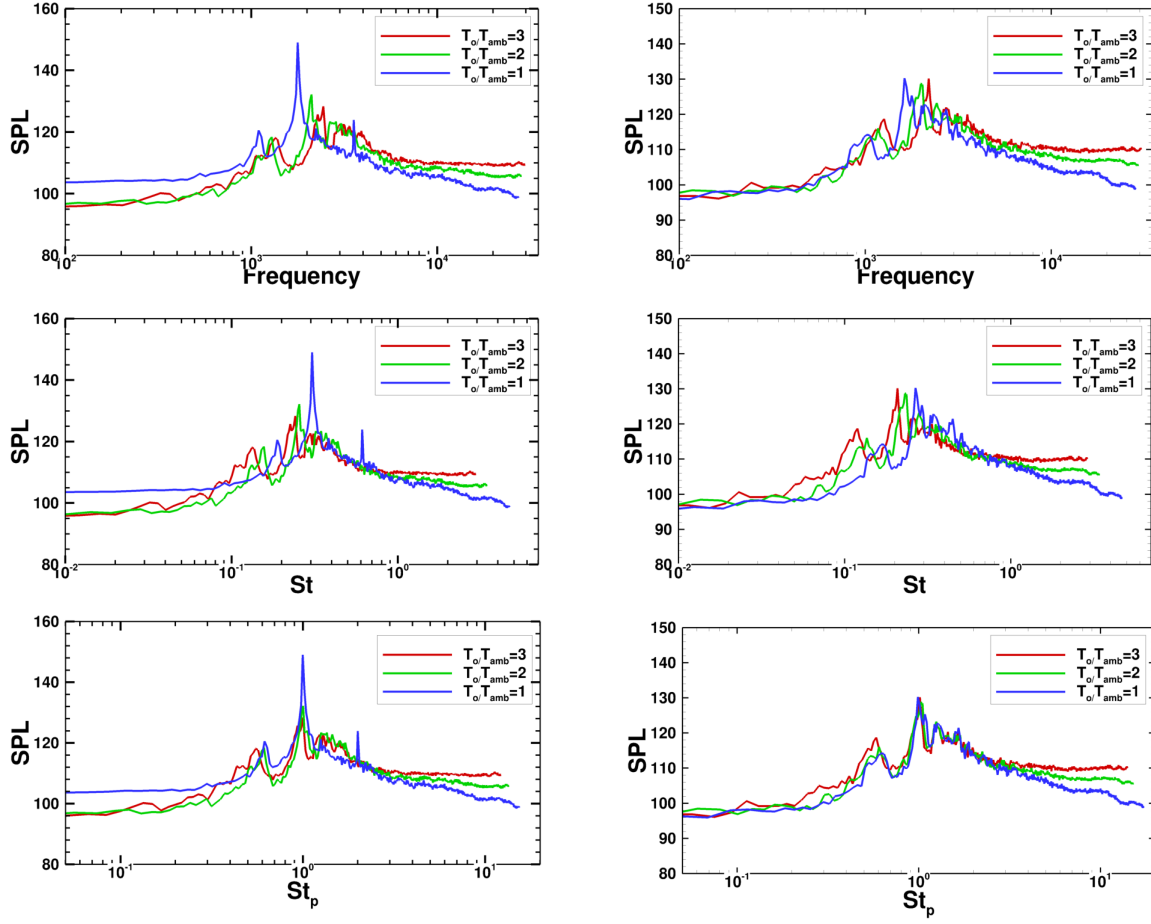


Figure 8. SPL distributions at 1.5D above the nozzle exit on the FW-H surface in both the overexpanded and an underexpanded cold jets. Figures on the left: overexpanded jet at $M_j = 1.47$. Figures on the right: Underexpanded jet at $M_j = 1.56$ from Ref. [18]. St_p is the Strouhal number normalized by the peak Strouhal number.

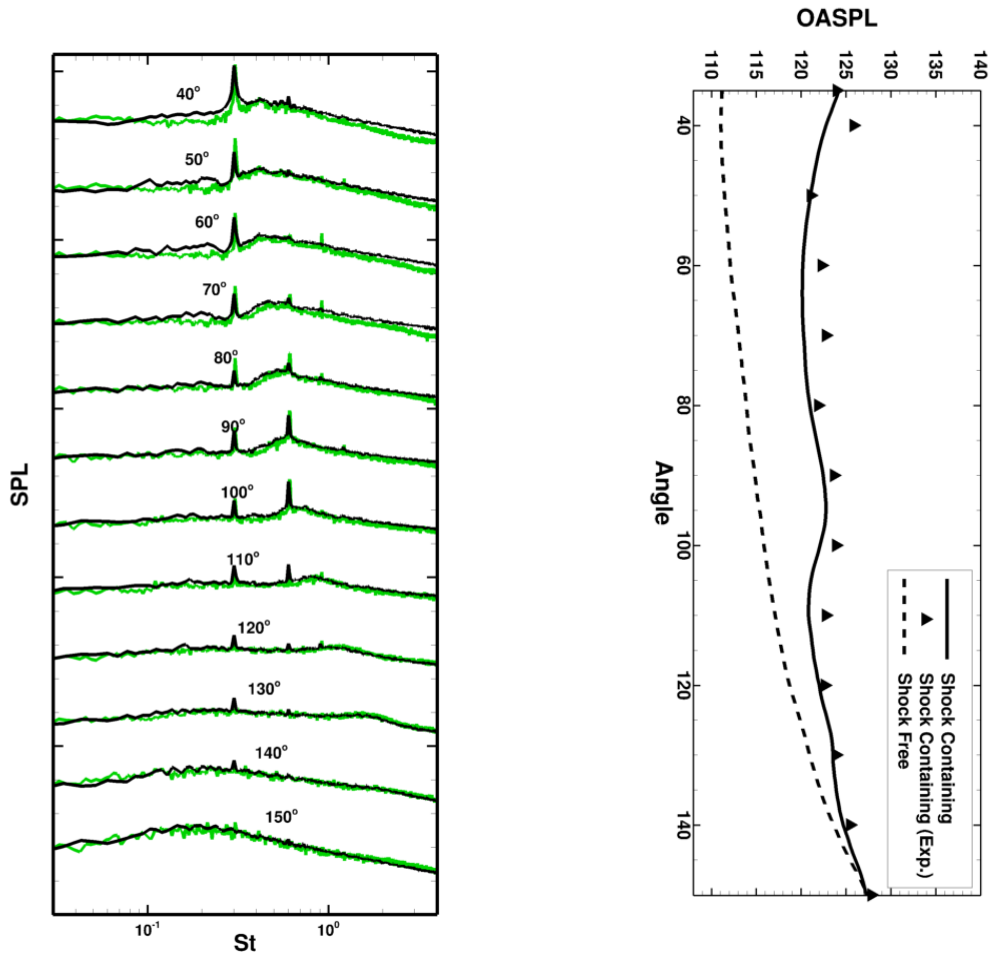


Figure 9. Far field sound noise distributions. Figure on the left is SPL distributions in the overexpanded jet flow. The radiation angle is from upstream to downstream. The green lines are LES results and black lines are measurement data. Figure on the right is far-field OASPL distributions of both overexpanded and shock-free jet flows.

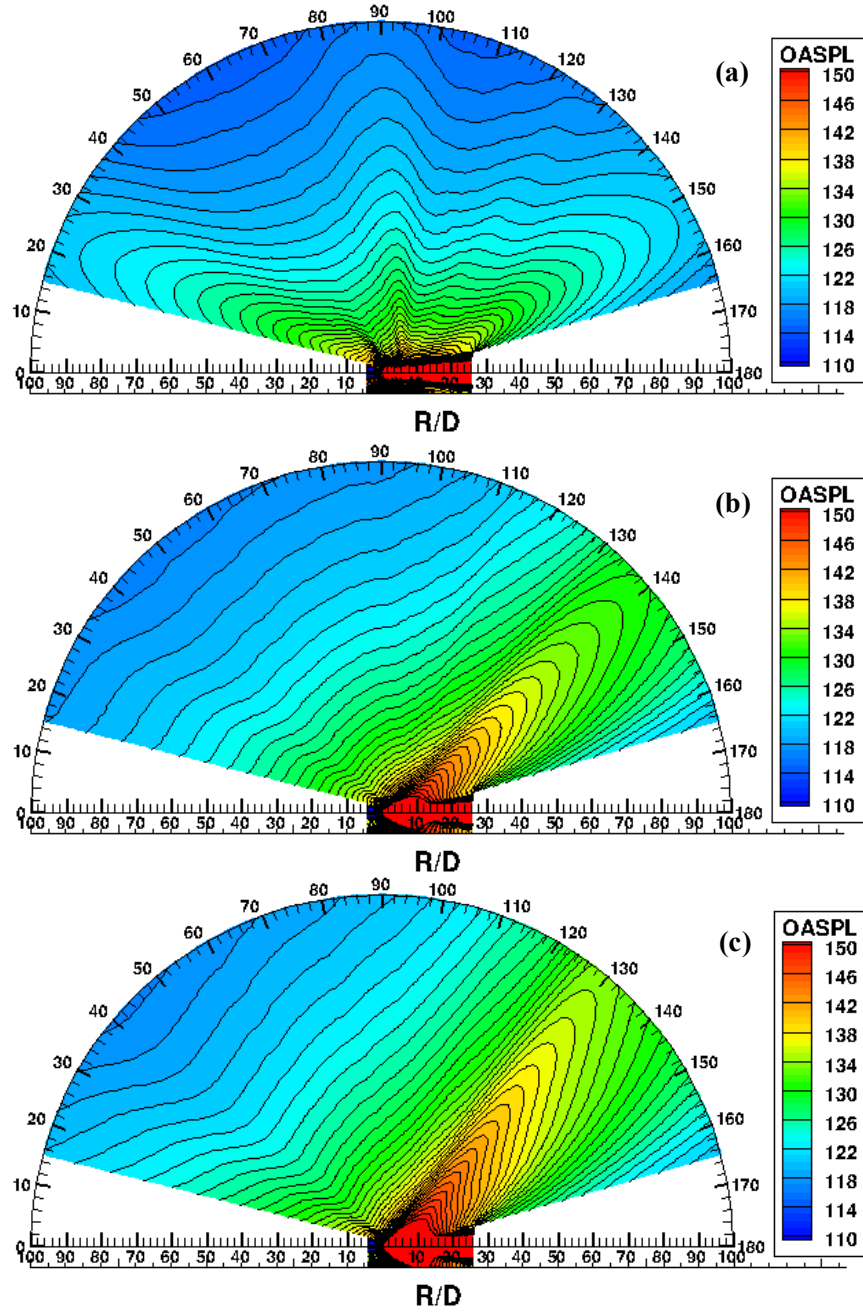


Figure 10. OASPL contours from the jet plume to a far-field distance of $r = 100D$. (a). $TTR = 1.0$. (b). $TTR = 2.0$. (c). $TTR = 3.0$.

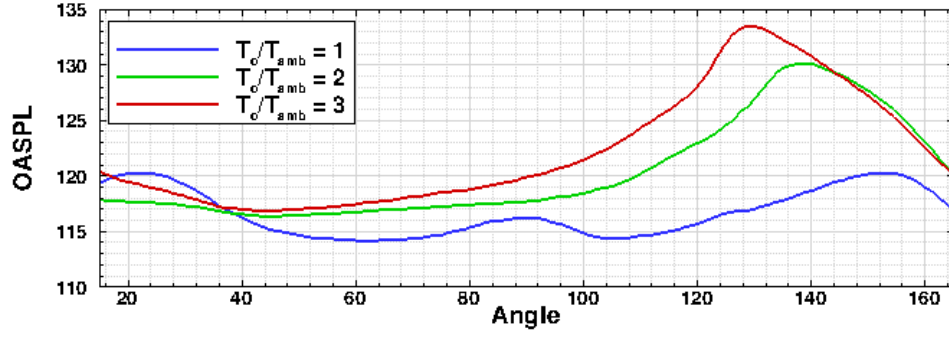


Figure 11. Far-field overall sound pressure levels at $r = 100D$.

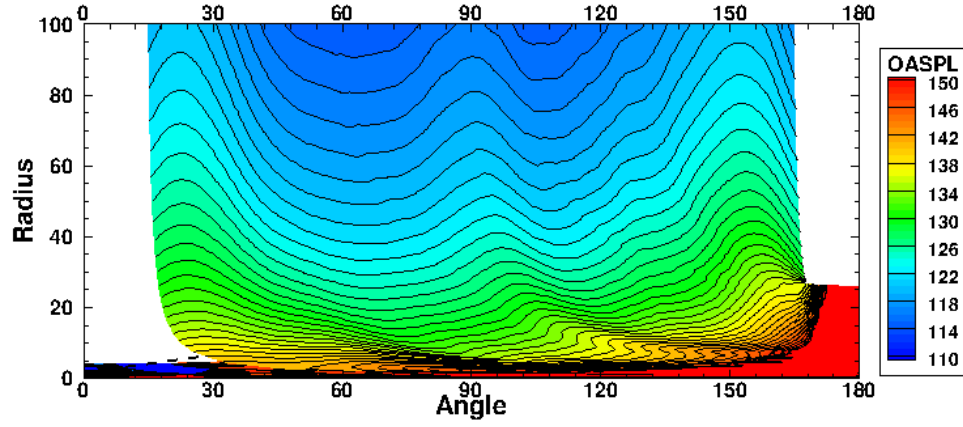


Figure 12. OASPL contours from the jet plume to a far-field distance of $r = 100D$ in the cold overexpanded jet.

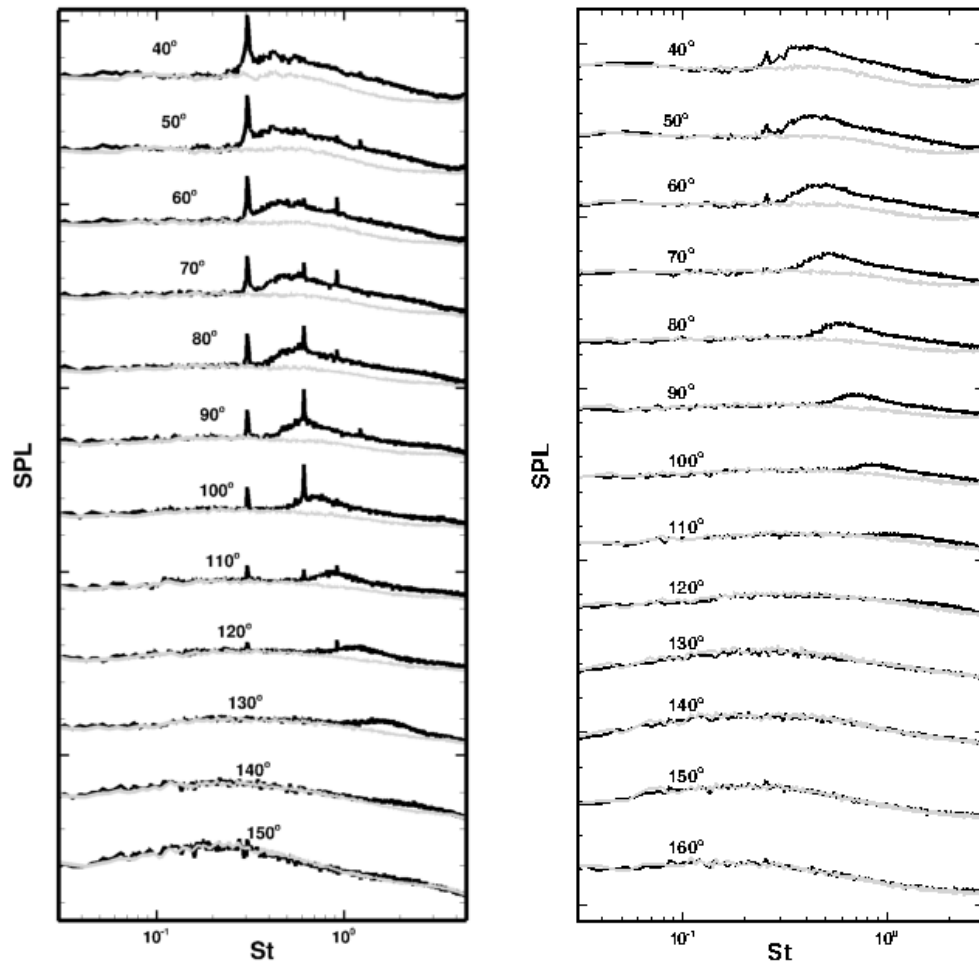


Figure 13. Far field sound pressure level distributions at jet conditions of $TTR = 1.0$ (left) and $TTR = 2.0$ (right). Dark lines: shock-containing jets. Gray lines: shock-free jets. The angle is from upstream to downstream.

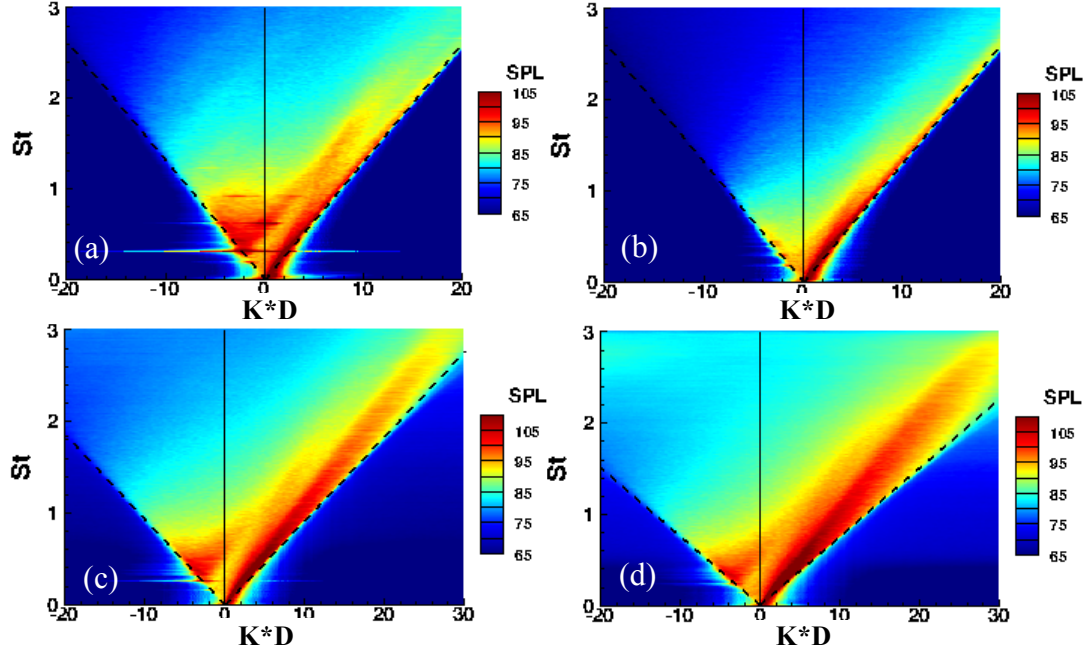


Figure 14. SPL distributions on the FW-H surface in the frequency-wavenumber space. “K” is the wavenumber. The left quadrant in each figure shows the upstream propagating waves and the right quadrant shows the downstream propagating waves. The dashed lines are the wave speed at the ambient sound speed. (a). Overexpanded jet of $TTR = 1.0$. (b). Shock-free jet of $TTR = 1.0$. (c). Overexpanded jet of $TTR = 2.0$. (d). Overexpanded jet of $TTR = 3.0$.

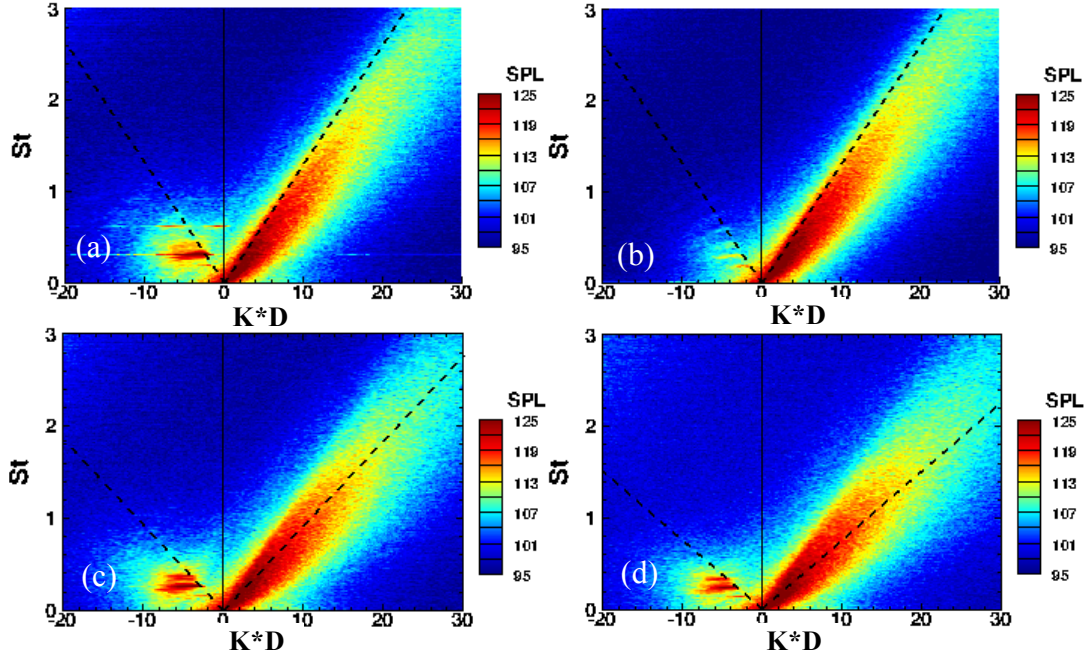


Figure 15. SPL distributions along the lip line in the frequency-wavenumber space. “K” is the wavenumber. The left quadrant in each figure shows the upstream propagating waves and the right quadrant shows the downstream propagating waves. The dashed lines are the wave speed at the ambient sound speed. (a). Overexpanded jet of $TTR = 1.0$. (b). Shock-free jet of $TTR = 1.0$. (c). Overexpanded jet of $TTR = 2.0$. (d). Overexpanded jet of $TTR = 3.0$.

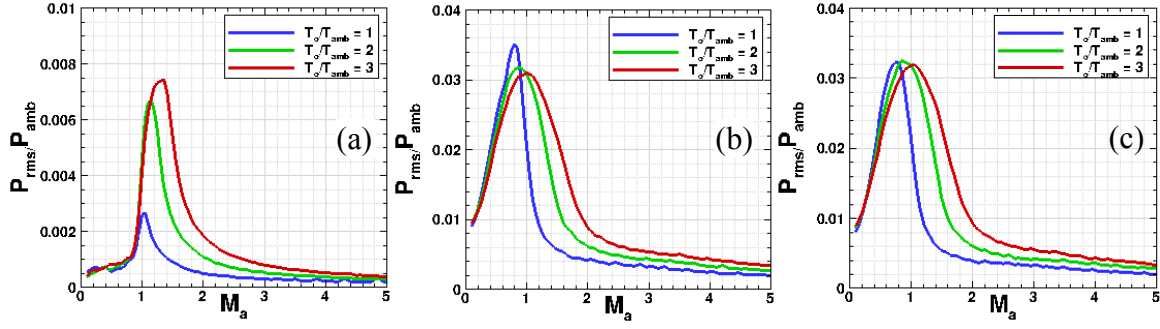


Figure 16. Pressure intensity of downstream propagating waves. (a). Overexpanded jets along the conical surface. (b). Overexpanded jets along the lip line. (c). Shock-free jets along the lip line. M_a is the acoustic Mach number $\frac{U_c}{a_{amb}}$, where U_c is the phase velocity of pressures waves traveling on either the conical surface or the lip line. a_{amb} is the ambient sound speed.

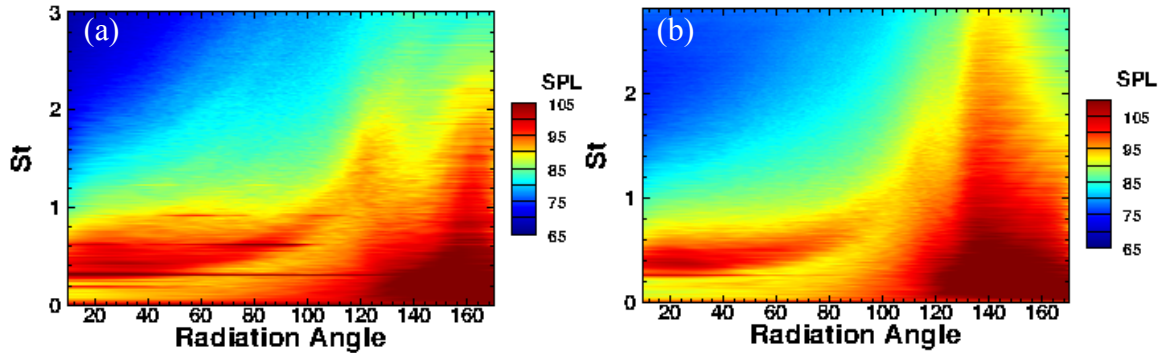


Figure 17. SPL distributions on the FW-H surface in the frequency-radiation angle space. (a). Overexpanded jet of $TTR = 1.0$ (b). Overexpanded jet of $TTR = 2.0$.

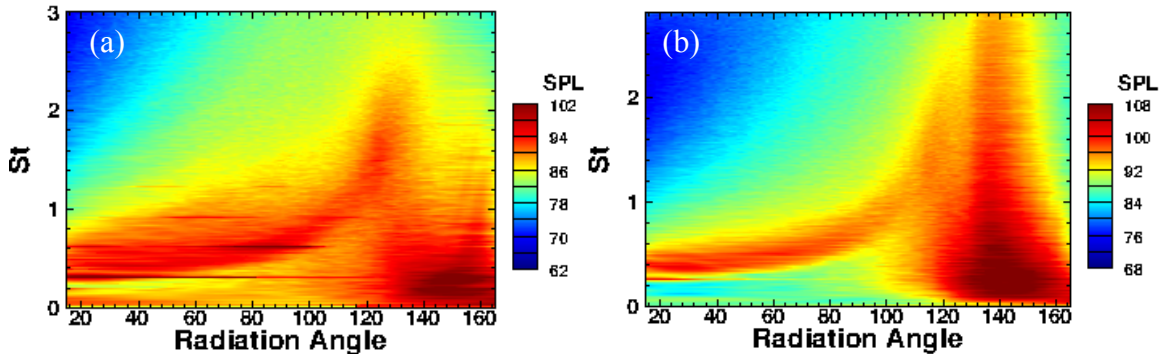


Figure 18. Far-field SPL distributions at $r = 100D$. (a). Overexpanded jet of $TTR = 1.0$. (b). Overexpanded jet of $TTR = 2.0$.

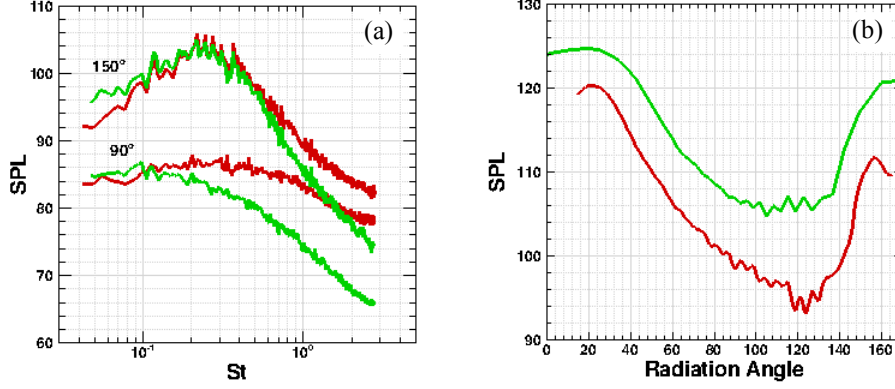


Figure 19. Comparison of the near-field and far-field SPL distributions. (a). SPL distributions at both 90° and the peak radiation angle in the shock-free cold jet. The near-field SPL levels are modified to match the far-field peak level. (b). SPL distributions at the fundamental screech frequency at $St = 0.305$ in the cold overexpanded jet. Green lines are the near-field data in **Figure 17(a)**, and the red lines are the far-field prediction at $r = 100D$ in **Figure 18(a)**.

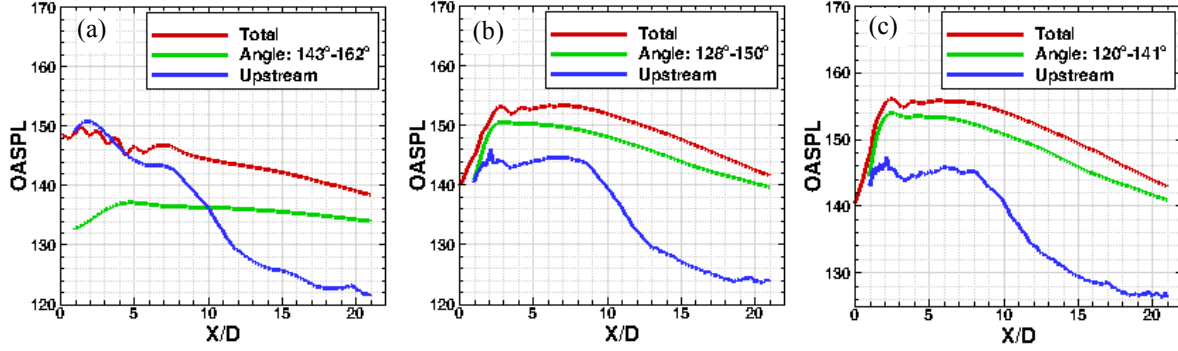


Figure 20. Axial distributions of pressure wave intensity $OASPL = 20 \log_{10} \left(\frac{p'}{p_{ref}} \right)$ of waves traveling on the FW-H surface. Downstream propagating waves associated with the Mach wave radiation and waves propagating upstream of 80.5° are also included. (a). $TTR = 1.0$. (b). $TTR = 2.0$. (c). $TTR = 3.0$.

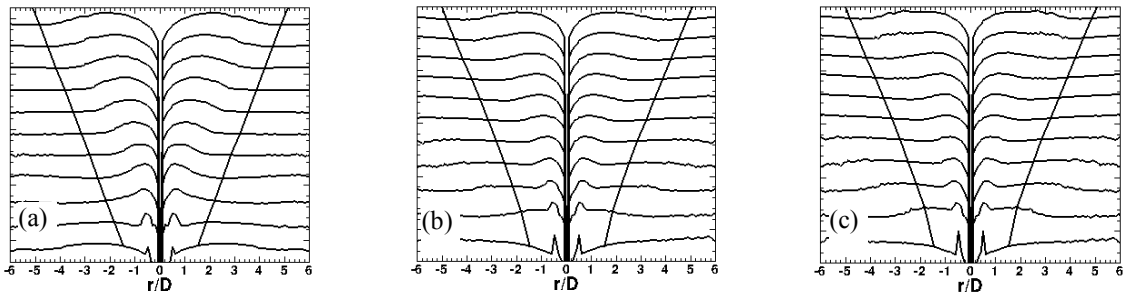


Figure 21. Radial profiles of $20 \log_{10} \left(\frac{p'}{p_{ref}} \cdot \frac{r}{D} \right)$ at multiple axial locations. Incrementing values are added to each profile to separate the curves. The two cross lines in each figure are the location of the FW-H surface. (a). $TTR = 1.0$. (b). $TTR = 2.0$. (c). $TTR = 3.0$.

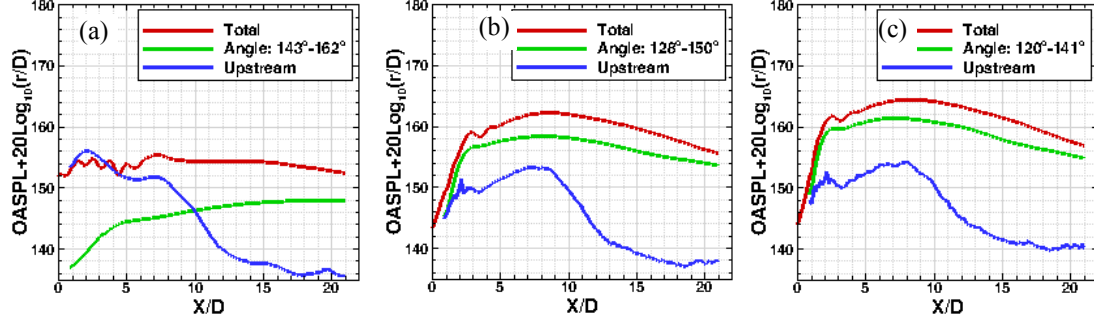


Figure 22. Axial distributions of the intensity $20\text{Log}_{10}(\frac{p'}{p_{ref}} \cdot \frac{r}{D})$ of pressure waves traveling on the conical surface. Downstream propagating waves propagate around the Mach wave radiation direction and waves propagating upstream of 80.5° are included. (a). $TTR = 1.0$. (b). $TTR = 2.0$. (c). $TTR = 3.0$.

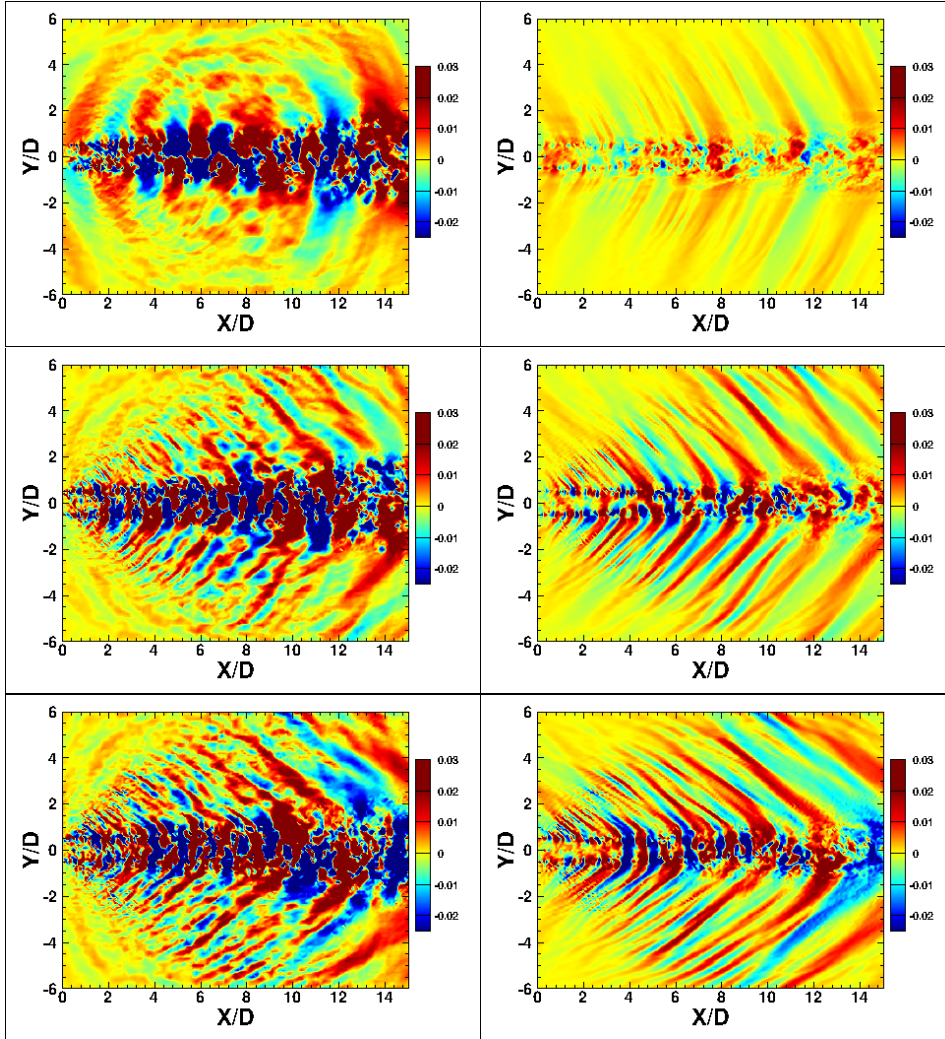


Figure 23. Instantaneous pressure fluctuation distributions. Figures on the right are the pressure fluctuations. Figures on the left are pressure fluctuations associated with the Mach wave radiations shown in **Figure 20**. Top: $TTR = 1.0$. Middle: $TTR = 2.0$. Bottom: $TTR = 3.0$.

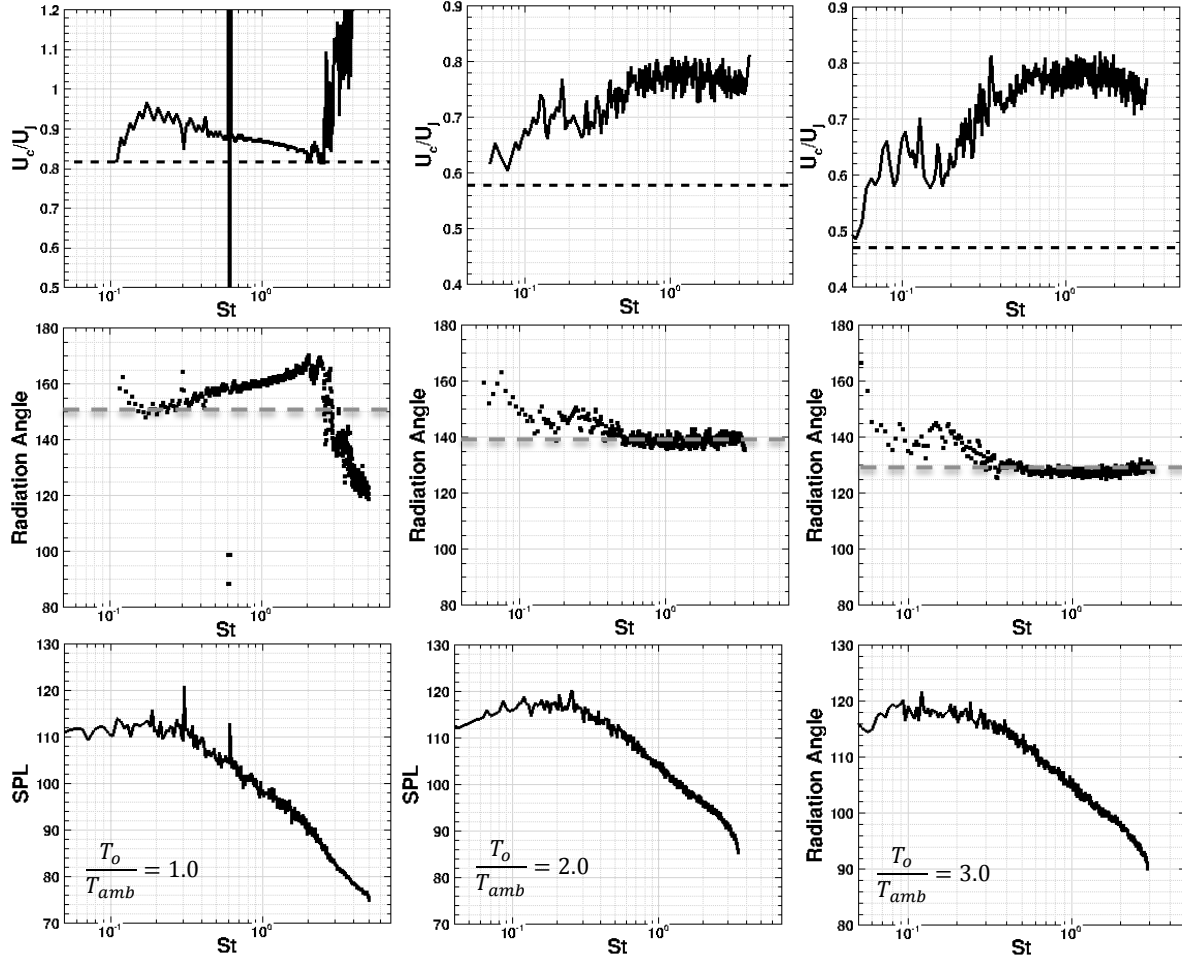


Figure 24. The frequency dependence of the peak phase velocity (top row), peak radiation angles (middle row), and peak SPL (bottom row) on the conical surface. The black dash lines are the locations of the ambient sound speed in the phase velocity profiles. The gray dash lines in the radiation direction profiles are the far-field peak radiation angles.

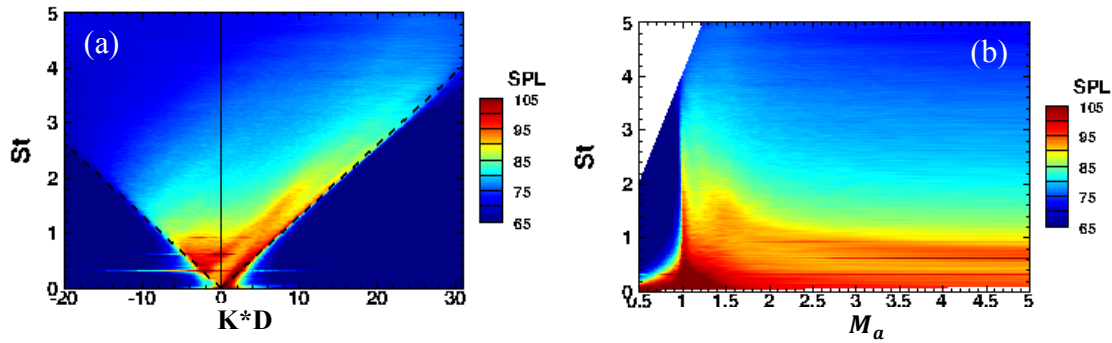


Figure 25. Wave intensity contours of pressure waves propagating downstream of 80.5° in the frequency and wave speed space. M_a is the acoustic Mach number of the wave speed.

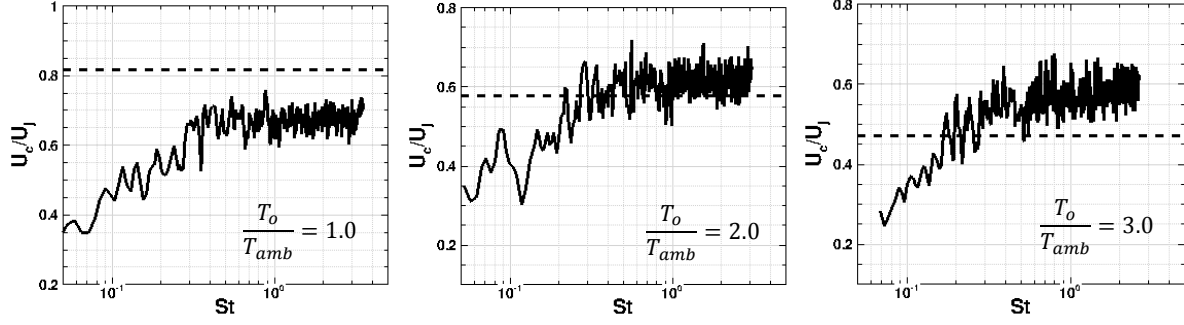


Figure 26. Frequency dependence of the peak convection velocities along the lip line. The dash lines are the location of the ambient sound speed.

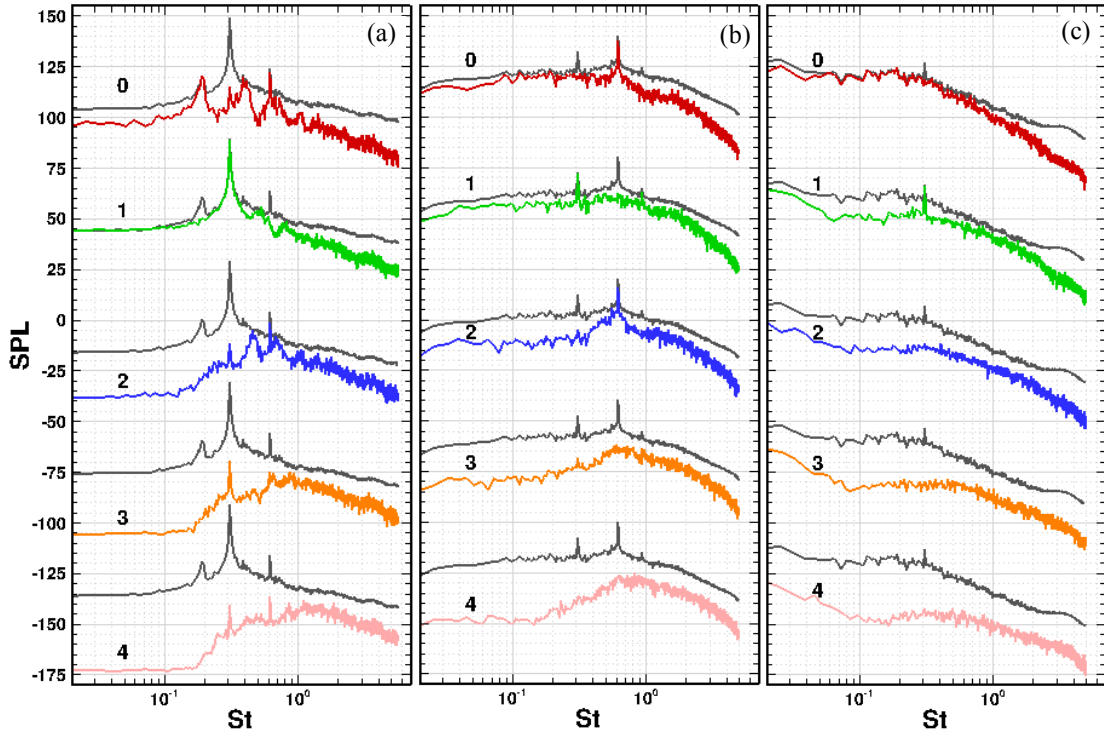


Figure 27. Pressure fluctuation intensities in azimuthal modes in the overexpanded cold jet. (a). At $x = 1.5D$ above the nozzle exit. (b). At $x = 7D$ and $r = 2.7D$. (c). At $x = 20D$ and $r = 4.8D$. Five modes are shown in each figure, and the distribution of each mode is plotted against that of the total intensity, which is shown as the grey lines.

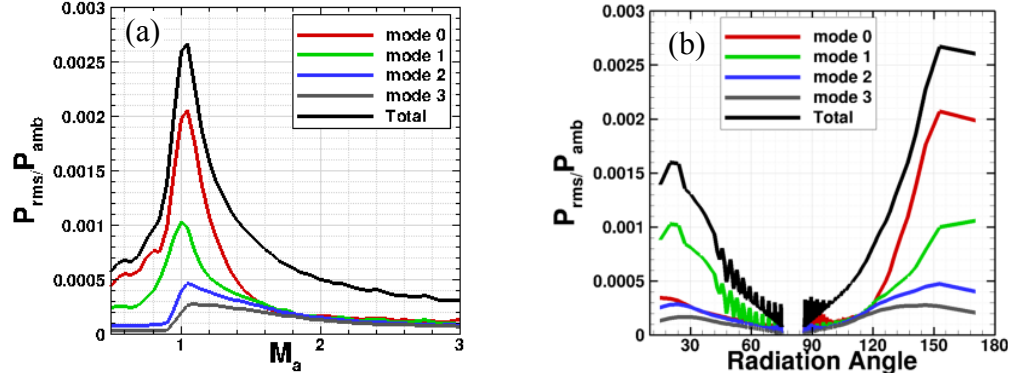


Figure 28. Azimuthal properties of pressure waves on the conical surface in the cold overexpanded jet. Results of four azimuthal modes are shown. (a). Pressure wave intensity versus the acoustic Mach number. Only waves propagating downstream of 80.5° are included. (b). Pressure wave intensity versus the radiation direction.

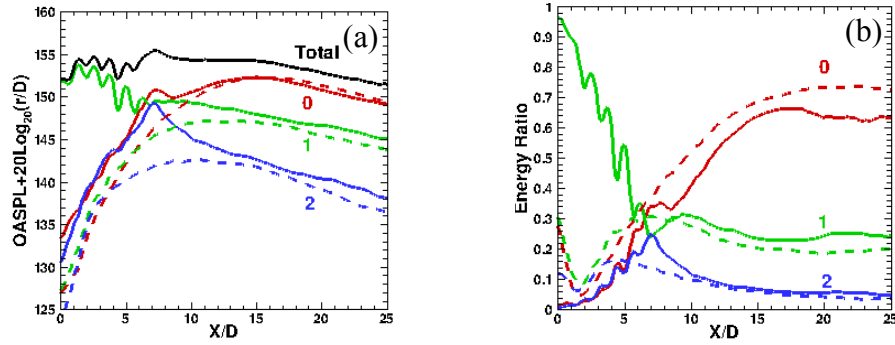


Figure 29. Pressure wave intensities along the conical surface of three azimuthal modes in the cold jets. (a). Intensities of the production $p'_m \cdot r$ ($m = 0, 1, 2$). (b). The ratio between the pressure wave intensity in each mode and the total intensity. Solid lines are the results from the overexpanded cold jet. Dashed lines are from the shock-free cold jet.

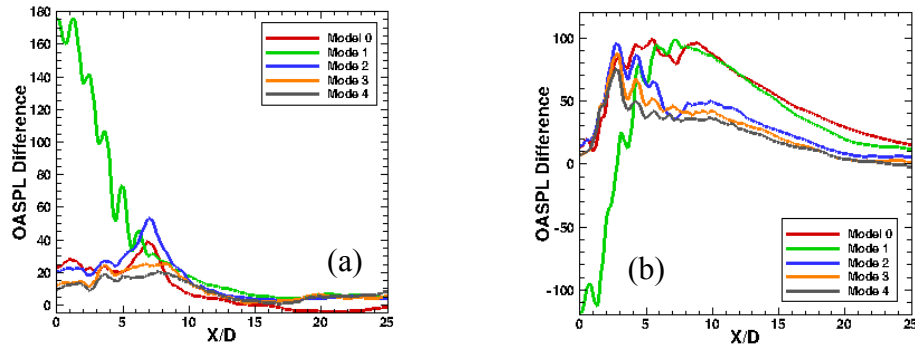


Figure 30. Impact of shock cells and heating on the noise intensity in the first five azimuthal modes. The intensity is computed as $10 \log_{10}((p'^2_m/P_{amb}^2) \cdot 10^{10})$. (a). The increase caused by shock cells in the cold overexpanded jet. (b). The increase caused by the heating effect as the jet temperature increases from $TTR = 1.0$ to $TTR = 2.0$.

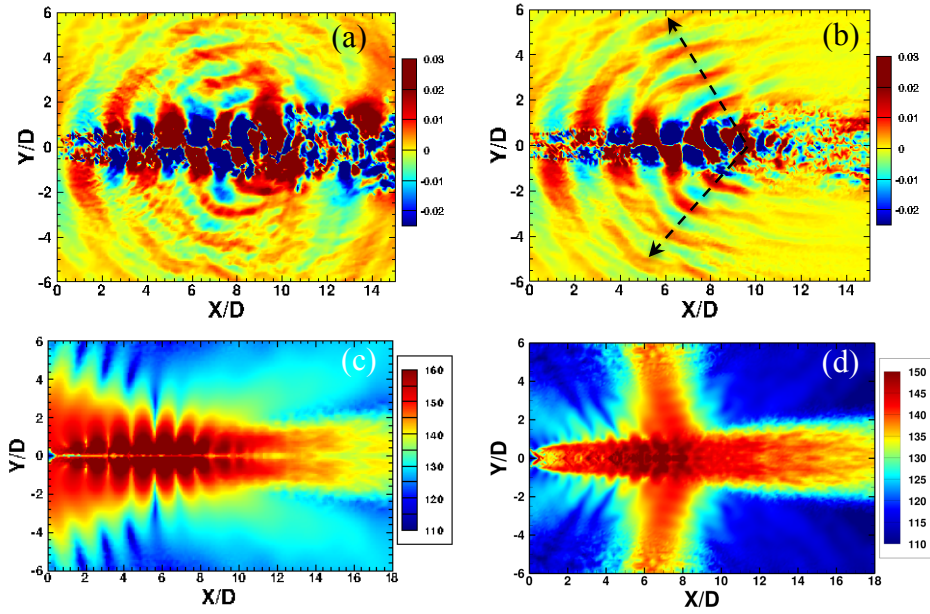


Figure 31. Instantaneous pressure fluctuations and SPL contours at screech frequencies in the cold jet. (a). Full pressure fluctuations. (b). Upstream propagating fluctuations. Arrows show the second screech harmonic waves. (c). SPL contours at the screech frequency of $St = 0.305$. (d). SPL contours at the second screech harmonic frequency of $St = 0.61$.

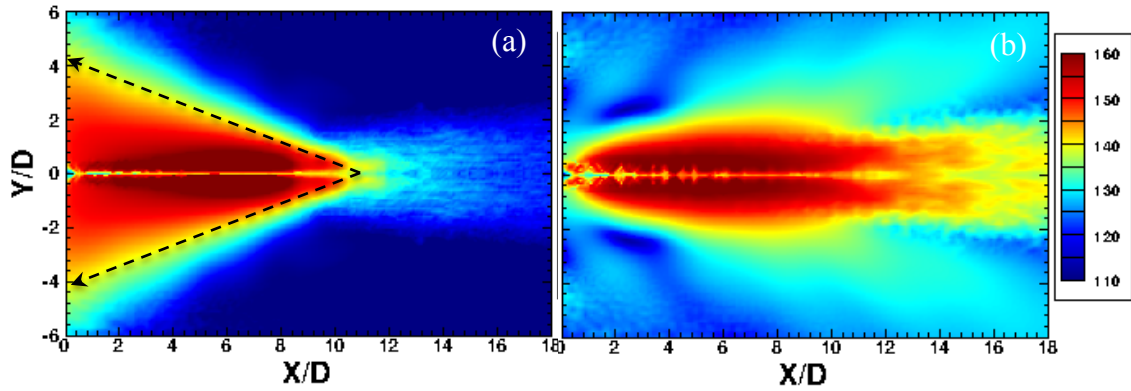


Figure 32. Pressure intensities at the screech frequency of $St = 0.301$ in the cold overexpanded jet. (a). Upstream propagating intensity distribution. The dash lines show the screech peak propagation direction. (b). Downstream propagating intensity distribution.

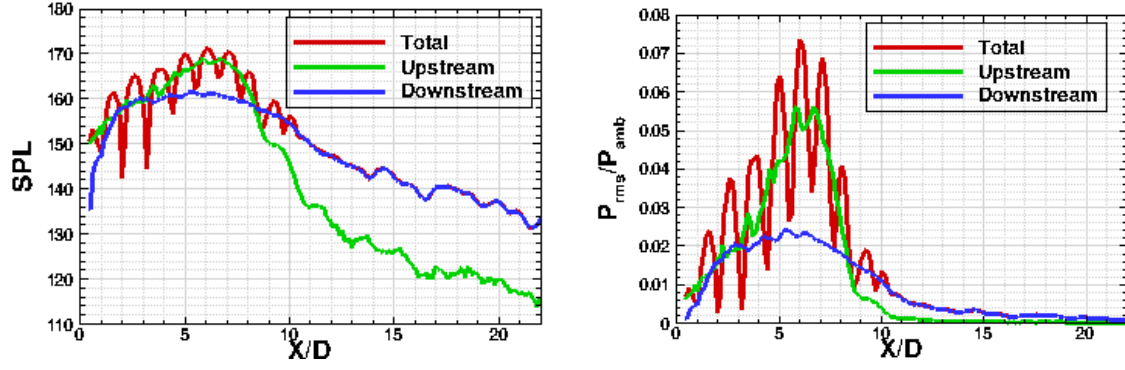


Figure 33. Lip-line pressure intensities at the screech frequency of $St = 0.301$ in the cold overexpanded jet. The intensities are plotted in two different scales.

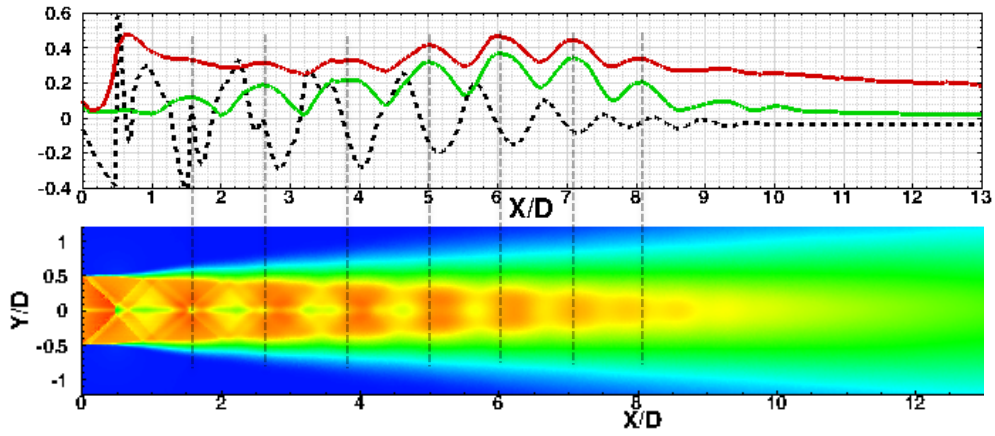


Figure 34. Top: Lip-line pressure fluctuation intensity p'/p_{amb} (red line) and the pressure intensity at the screech frequency of $St = 0.305$ (green line) versus the centerline static pressure distribution $p/p_{atm} - 1$ (dash line). The pressure intensity and screech intensity are multiplied by 5. Bottom: time-averaged axial velocity distribution. Straight dash lines are the peak intensity locations.

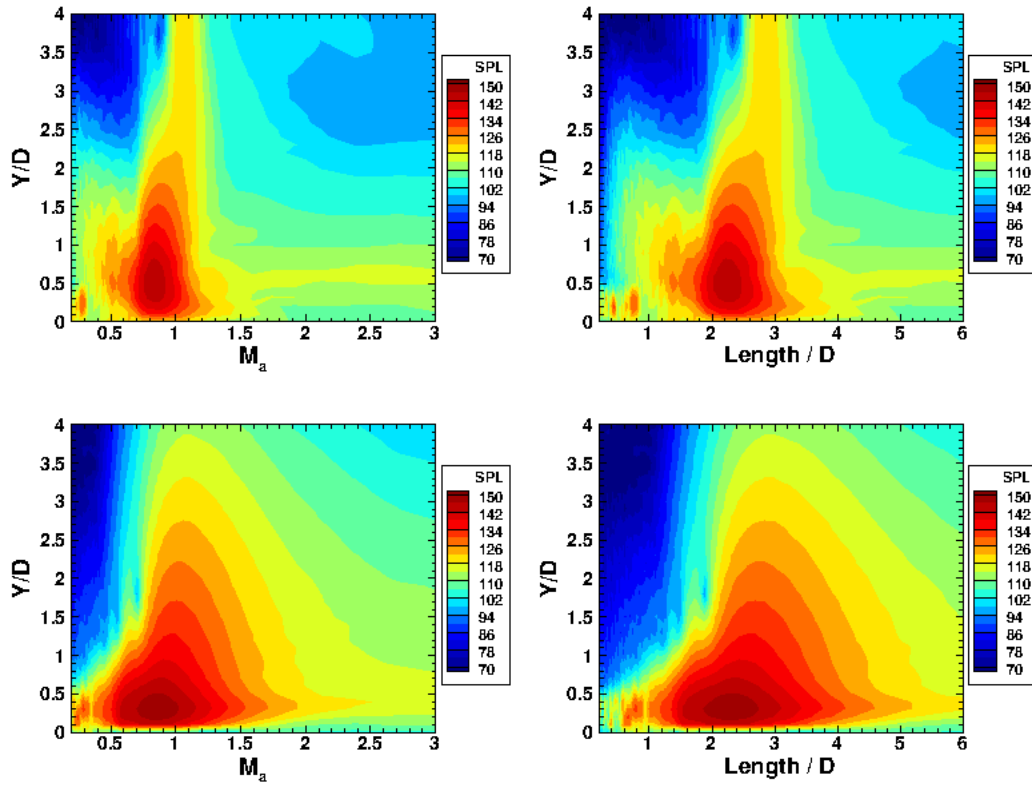


Figure 35. Pressure intensity versus acoustic Mach number and the length scale at the screech frequency in the radial direction in the overexpanded cold jet. (a)-(b). Downstream propagating waves. (c)-(d). Upstream propagating waves.

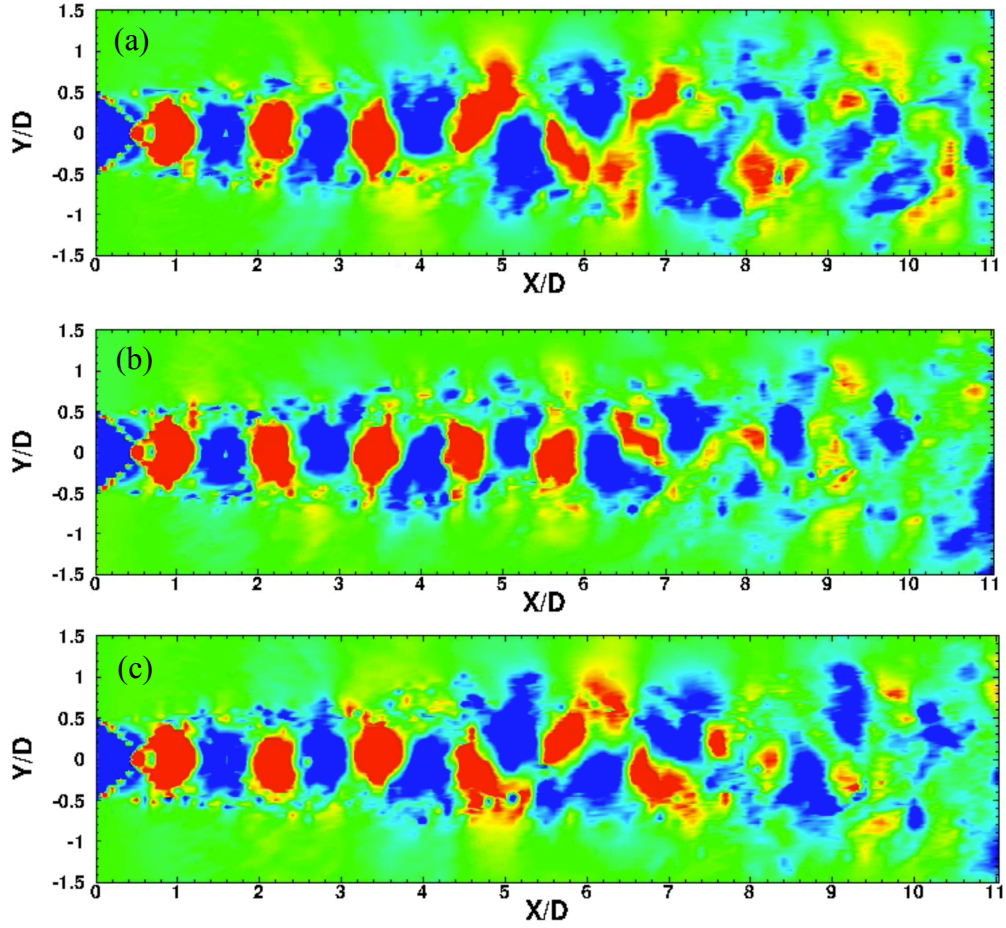


Figure 36. Shock-cell oscillations in the cold overexpanded jet. The contour magnitude is between $0.9P_{\text{atm}}$ and $1.1P_{\text{atm}}$. (a). The 5th shock cell moves down towards the lip line and rotates in a counterclockwise direction, but its neighboring compression waves (the 4th and 6th shock cells) oscillate at opposite directions. (b). Shock cells moves back to the location near the jet axis. (c). The 5th compression wave moves up towards the lip line and rotates in a clockwise direction, but its neighboring compression waves oscillate at opposite directions.

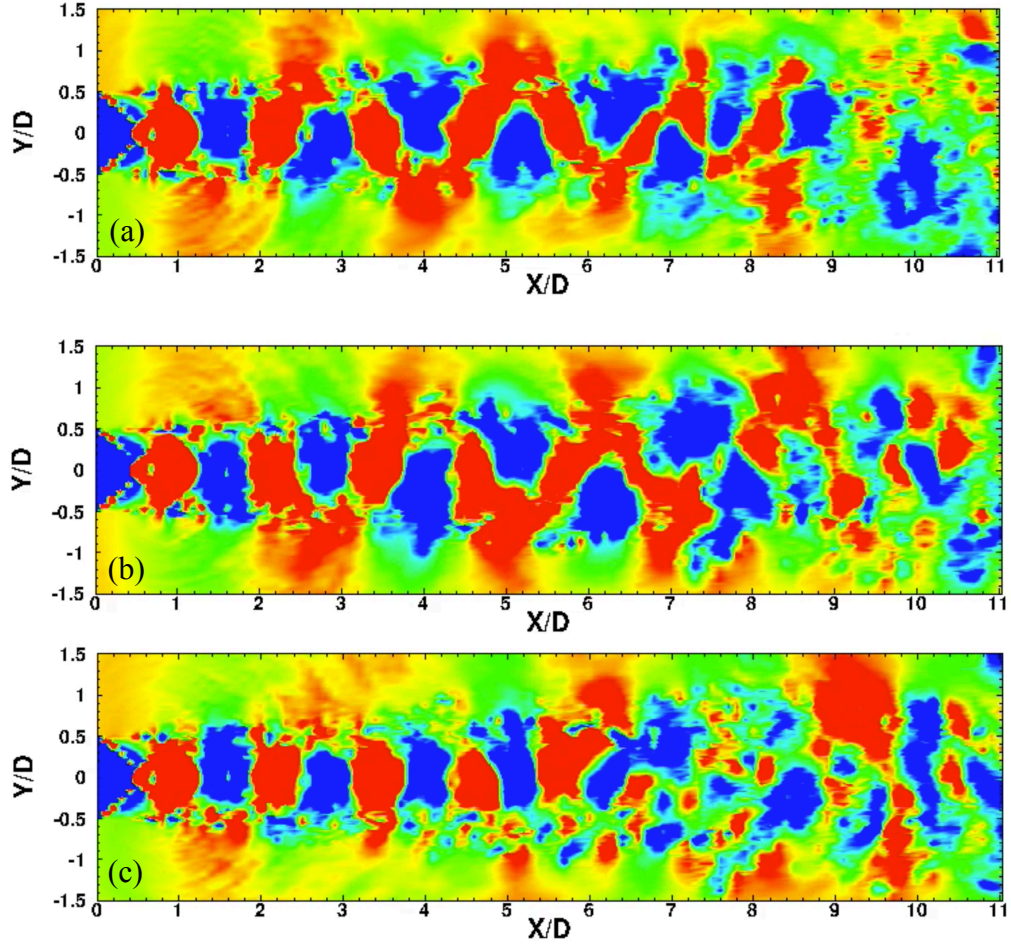


Figure 37. The generation of high-intensity pressure waves in the cold overexpanded jet. The contour magnitude is between $0.92P_{\text{atm}}$ and $1.02P_{\text{atm}}$. (a)&(b). High-intensity pressure waves are observed when two neighboring compression waves rotate at an opposite direction and the edges of those pressure waves get close to each other near the lip line. (c). Shock cells move back to the location near the jet axis and high-intensity waves are mostly absent at this shock-cell position.

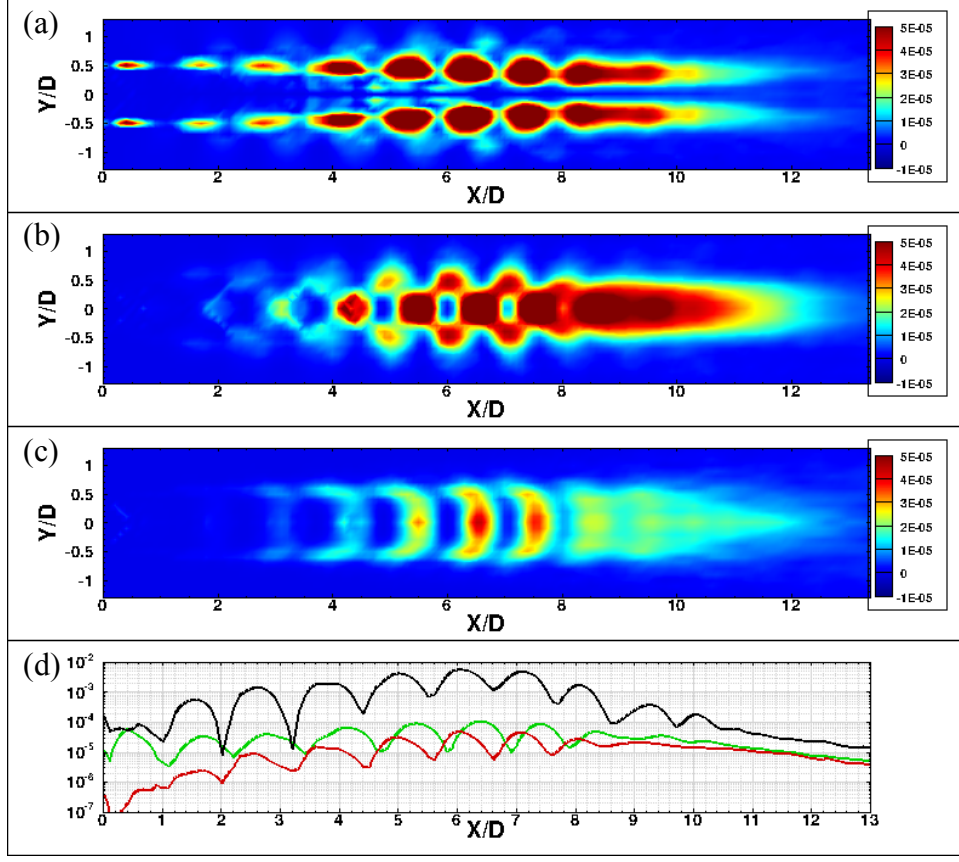


Figure 38. Turbulence fluctuation intensities at the screech frequency of $St = 0.305$ in the cold jet. (a). u'^2/U_j^2 . (b). v'^2/U_j^2 . (c). w'^2/U_j^2 . (d). Intensities along the lip line. p'^2/P_{atm}^2 (black line), v'^2/U_j^2 (red line) and u'^2/U_j^2 (green line).

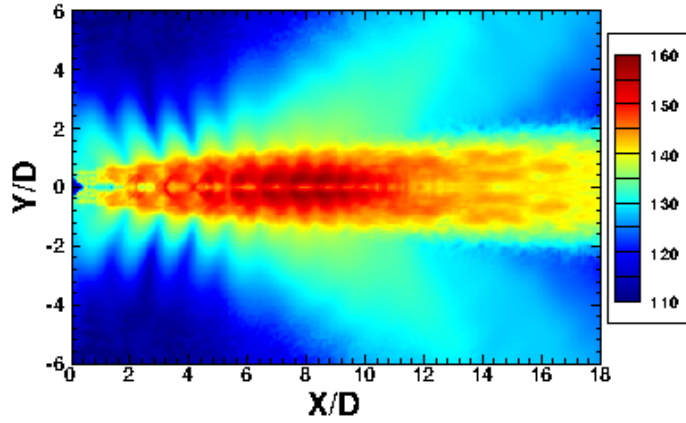


Figure 39. Pressure fluctuation intensities at the screech frequency of $St = 0.26$ in the heated jet of $TTR = 2.0$.

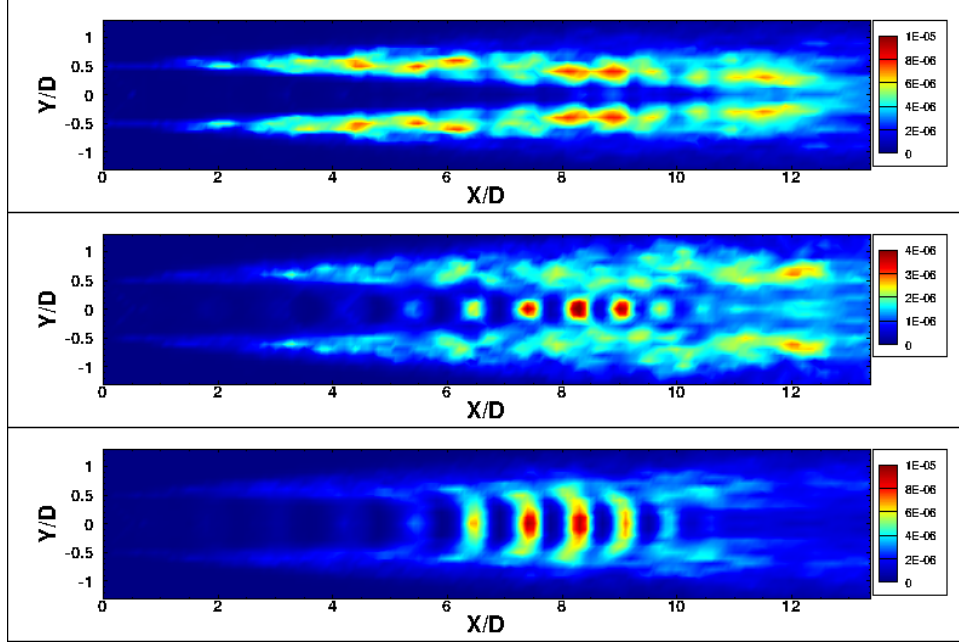


Figure 40. Turbulence fluctuation intensities at the screech frequency of $St = 0.26$ in the heated jet of $TTR = 2$. (a). u'^2/U_j^2 . (b). v'^2/U_j^2 . (c). w'^2/U_j^2 .

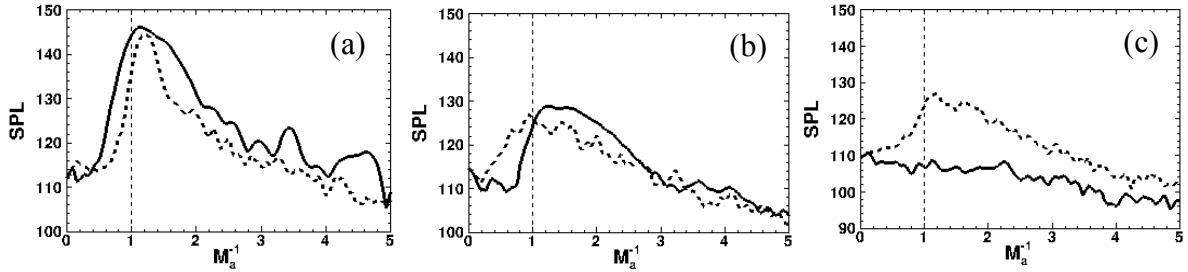


Figure 41. Upstream and downstream propagating pressure intensities versus the inverse of the acoustic Mach number along the lip line. Solid lines: upstream propagating waves. Dash lines: downstream propagating waves. (a). Cold overexpanded jet. (b) A heated overexpanded jet at $TTR = 2.0$. (c). Cold shock-free jet.

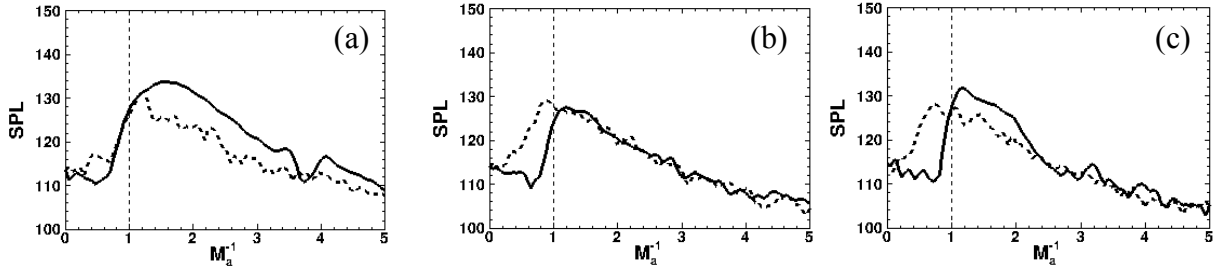


Figure 42. Upstream and downstream propagating pressure intensities versus the inverse of the acoustic Mach number along the lip line in underexpanded jets reported in Ref. [18]. Solid lines: upstream propagating waves. Dash lines: downstream propagating waves. (a). Cold underexpanded jet. (b) A heated underexpanded jet at $TTR = 2.0$. (c). A heated underexpanded jet at $TTR = 3.0$.

